Ore Geology Reviews 76 (2016) 79–93

Contents lists available at ScienceDirect

Ore Geology Reviews

journal homepage: www.elsevier.com/locate/oregeorev

Geology and genesis of the Xiaguan Ag–Pb–Zn orefield in Qinling orogen, Henan province, China: Fluid inclusion and isotope constraints

Jing Zhang [a,*], Yanjing Chen [b], Qiangwei Su [a], Xu Zhang [c], Shihong Xiang [c], Qisong Wang [a]

[a] State Key Laboratory of Geological Processes and Mineral Resources, China University of Geosciences, Beijing 100083, China
[b] Open Laboratory of Orogenic and Crustal Evolution, Peking University, Beijing 100871, China
[c] Henan Provincial Non-ferrous Metals Geological and Mineral Resources Bureau, Zhengzhou 450016, China

ARTICLE INFO

Article history:
Received 10 April 2015
Received in revised form 11 January 2016
Accepted 11 January 2016
Available online 13 January 2016

Keywords:
Xiaguan Ag–Pb–Zn orefield
Geology and geochemistry
CMF model
Orogenic-type deposits
Qinling orogen

ABSTRACT

The Xiaguan Ag–Pb–Zn orefield (Neixiang County, Henan Province), hosting the Yindonggou, Zhouzhuang, Yinhulugou and Laozhuang fault-controlled lode deposits, is situated in the Erlangping Terrane, eastern Qinling Orogen. The quartz-sulfide vein mineralization is dominated by main alteration styles of silicic-, sericite-, carbonate-, chlorite- and sulfide alteration. Major Ag-bearing minerals are freibergite, argentite and native Ag. The deposits were formed by a CO_2-rich, mesothermal (ca. 250–320 °C), low-density and low salinity (<11 wt.% NaCl equiv.), Na^+–Cl^--type fluid system. Trapping pressures of the carbonic-type fluid inclusions (FIs) decreased from ca. 280–320 MPa in the early mineralization stage to ca. 90–92 MPa in the late mineralization stage, indicating that the ore-forming depths had become progressively shallower. This further suggests that the metallogenesis may have occurred in a tectonic transition from compression to extension. Geological- and ore fluid characteristics suggest that the Xiaguan Ag–Pb–Zn orefield belongs to orogenic-type systems.

The $\delta^{18}O_{H2O}$ values change from the Early (E)-stage (7.8–10.8 ‰), through Middle (M)-stage (6.0–9.4 ‰) to Late (L)-stage (−1.5–3.3 ‰), with δD values changing from E-stage −95 to −46 ‰, through M-stage −82 to −70 ‰ to L-stage −95 to −82 ‰. $\delta^{13}C_{CO2}$ values of the ore fluids in the E- and M-stage quartz vary between 0.1 ‰ and 0.9 ‰ (average: 0.3 ‰); $\delta^{13}C_{CO2}$ values of L-stage FIs are −0.2–0.1 ‰ in quartz and −6.8 ‰ to −3.5 ‰ in calcite. The H–O–C isotopic data indicate that the initial ore fluids were sourced from the underthrusted Qinling Group marine carbonates, and were then interacted with the ore-hosting Erlangping Group metasedimentary rocks. Inflow of circulated meteoric water may have dominated the L-stage fluid evolution.

Sulfur ($\delta^{34}S$ = 1.9–8.1 ‰) and lead isotopic compositions ($^{206}Pb/^{204}Pb$ = 18.202–18.446, $^{207}Pb/^{204}Pb$ = 15.567–15.773 and $^{208}Pb/^{204}Pb$ = 38.491–39.089) of sulfides suggest that the ore-forming materials were mainly sourced from the ore-hosting metasedimentary strata. The stepped heating sericite $^{40}Ar/^{39}Ar$ detection suggests that the mineralization occurred in the Middle Jurassic to Early Cretaceous (ca. 187−124 Ma). Considering the regional tectonic evolution of the Erlangping Terrane, we propose that the Xiaguan Ag–Pb–Zn orefield was formed in a continent–continent collisional tectonic regime, in accordance with the tectonic model for continental collision, metallogeny and fluid flow (CMF).

1. Introduction

The Qinling Orogen constitutes an important part of the Central China Orogenic Belt and hosts several metallogenic provinces and belts, including the largest molybdenum belt (Li et al., 2007, 2011; Ni et al., 2012), the 2nd largest Carlin-type /−like Au province (Zhang et al., 2014) and the 3rd largest Hg–Sb belt (Tu and Ding, 1986) in the world, as well as China's largest orogenic-type Ag–(Pb–Zn) province (Chen et al., 2004, 2009) and 2nd largest orogenic gold province (Chen et al., 2009; Zhao et al., 2011; Deng et al., 2014a, 2015).

The Qinling Orogen records of a complex geological and tectonic history, including continental rifting, ocean basins opening and closure along convergent margins, continental growth and recycling, continental collision and intraplate tectonics (Chen and Fu, 1992; Zhao et al., 2004; Chen et al., 2009; Zhai and Santosh, 2013; Nance et al., 2014; Deng and Wang, 2015). Based on the mineralization during continent–continent collision, a tectonic model for collisional orogeny, metallogeny and fluid flow (CMF model) has been established to interpret the relationships between A-type subduction, ore-hosting structures, granitoids and porphyries genesis (Chen and Fu, 1992; Chen et al., 2004; Pirajno, 2009, 2013). According to the CMF model, zonation of three mineralization styles can be distinguished in the obducted plate, i.e., hydrothermal lode deposits (D zone), granites and their related deposits (G zone) and porphyries, breccia pipes and their related

* Corresponding author.
E-mail addresses: zhangjing@cugb.edu.cn, 19914013@sina.com (J. Zhang).

http://dx.doi.org/10.1016/j.oregeorev.2016.01.003
0169-1368/

deposits (P zone). The CMF model has not only interpreted the spatial and temporal pattern of regional mineralization (Chen et al., 2001, 2005; Chen, 2006), but also introduced the Xiaguan Ag polymetallic field as an exploration target in the D zone in eastern Qinling Orogen (Chen and Fu, 1992), which has been supported by geological exploration since 1999. However, both epithermal- and orogenic deposits, including Au, Ag, Hg, Sb, Pb, Zn, As, and Mo deposits, can occur in the D zone, which make the genesis and metallogenesis background of Xiaguan Ag polymetallic orefield complicated.

The Xiaguan Ag polymetallic field, located in Neixiang county, Henan province, is dominated by several Ag–Pb–Zn deposits and Au deposits, such as the Banchang Au–(Cu) and Xuyaogou Au deposits. In the Xiaguan Ag–Pb–Zn orefield, the Yindonggou deposit was discovered in 1999 and was proven to contain ~1300 t Ag, 0.154 Mt. Pb + Zn, and 9.7 t Au (HINME, Henan Institute of Nonferrous Metal Exploration, 2003; Wang et al., 2003). In the exploration around Yindonggou deposit, the medium Zhouzhuang Ag–Pb–Zn deposit (424 t Ag, 0.056 Mt. Pb + Zn, 2.3 t Au), and several small Ag–Au-dominated polymetallic deposits were also discovered at Lujiaping, Tumuya, Yinhulugou, Xiajiagou and Laozhuang (Cao et al., 2011; Fu et al., 2011; Xiang et al., 2012).

In this paper, we report the geological, fluid inclusion, H–O–C–S–Pb isotope geochemical data and Ar–Ar geochronology of the Xiaguan Ag–Pb–Zn orefield, discuss its metallogeny and sources of ore-forming materials and fluids. We suggest that ore deposits in the Xiaguan Ag–Pb–Zn orefield belong to the fault-controlled vein orogenic-type and may have formed under a continent–continent collisional setting.

2. Geological setting

2.1. Regional geology

The Qinling Orogen lies in the central part of the Central China Orogenic Belt (CCOB), which has evolved from the northernmost Paleo-Tethys Ocean and shaped up through the Mesozoic collision between the North China Craton and other Gondwana-derived blocks, e.g., the Yangtze Craton (Fig. 1A and B; Chen et al., 2009; Dong et al., 2011; Li et al., 2011; Goldfarb et al., 2014). The Qinling Orogen includes four distinct tectonic units, namely (from north to south) the Huaxiong Block (representing the reactivated southern North China Craton margin), Northern Qinling accretionary belt, Southern Qinling orogenic belt, and the Songpan foreland fold-thrust belt along the northern Yangtze margin. The San-Bao, Luanchuan, Shang-Dan, Mian-Lue and Longmenshan faults define the boundaries of these four tectonic units (Fig. 1B; Chen et al., 2009; Li et al., 2015).

The Northern Qinling accretionary belt includes the Qinling Metamorphic Complex, the Erlangping and Kuanping terranes. The Qinling Metamorphic Complex, also called the Qinling Group, comprises a pre-Rodinian metamorphic basement and Neoproterozoic — Paleozoic (mostly arc-related) granitoids (Fig. 2A). The Erlangping Terrane is bounded by the Zhu-Xia fault to the south and the Waxuezi fault to the north (Fig. 2A), and comprises mainly Neoproterozoic — Early Paleozoic backarc basin volcano-sedimentary successions and associated intrusions (Chen and Fu, 1992; Dong et al., 2013; Wang et al., 2014). In the Kuanping Terrane, the Kuanping Group consists mainly of Mesoproterozoic muscovite-biotite (quartz) schists, meta-gabbros, basaltic rocks and ophiolite slices, and is interpreted as an ophiolite complex accreted to the southern margin of the North China Craton (Hu et al., 1988; Chen et al., 2004; Wang et al., 2014).

2.2. Local geology

The Xiaguan Ag–Au polymetallic field is located in the Erlangping Terrane, which contains the Erlangping Group that comprises three units (from bottom to top), i.e., the Damiao, Huoshenmiao and Xiaozhai formations (Fig. 2A) (Hu et al., 1988; HBGR, Henan Bureau of Geology and Resource, 1989). The Xiaozhai Formation consists mainly of sericite quartz schist, biotite (muscovite) quartz schist, biotite (sericite) plagioclase schist, with their protoliths being flysch and carbonate interbeds (Wang et al., 2003). The Huoshenmiao and Damiao formations comprise spilite–keratophyre and gabbroic rocks.

These lithostratigraphic units were intruded by multiphase granitoids (Fig. 2A and B), such as the Muhuding granite (482 ± 30 Ma, Rb-Sr isochron age, Wei et al., 2003), Manziying granite (459.5 ± 0.7 Ma, zircon U–Pb age, Guo et al., 2010), Lujiaping granite (446 ± 7 Ma, zircon U–Pb age, Li et al., 2012), buried Songduo granite (ca. 190 — 140 Ma, Wang et al., 2003) and Erlangping biotite monzonitic granite (ca. 140 Ma, Rb-Sr isochron age, Chen et al., 1996).

In Xiaguan, most deposits and mineralization occurrences are hosted by the Xiaozhai biotite quartz schist and biotite (sericite) plagioclase schist and the Huoshenmiao spilite–keratophyre and gabbro (Fig. 2A).

3. Deposit geology

3.1. Orebody characteristics

A total of 53 Ag–Pb–Zn mineralization zones were delineated in the Xiaguan orefield and 39 of them have been proven economic (Tables 1 and 2, Wang et al., 2001; Xiang et al., 2012). These orebodies are NE-, N — S-, E — W- or NW-trending, and controlled by the subsidiary structures of the Zhu — Xia fault (Wang et al., 2003). North- to NE-trending veins dominate (Fig. 2), including the Y1, Y2, Y3 and Y10 orebodies at Yindonggou and the Z1 and Z2 orebodies at Zhouzhuang. Less important are the E — W- and NW-trending orebodies, such as Y4 and Y6 at Yindonggou, T3, T8 and T12 at Tumuya, and Z13 and Z14 at Zhouzhuang.

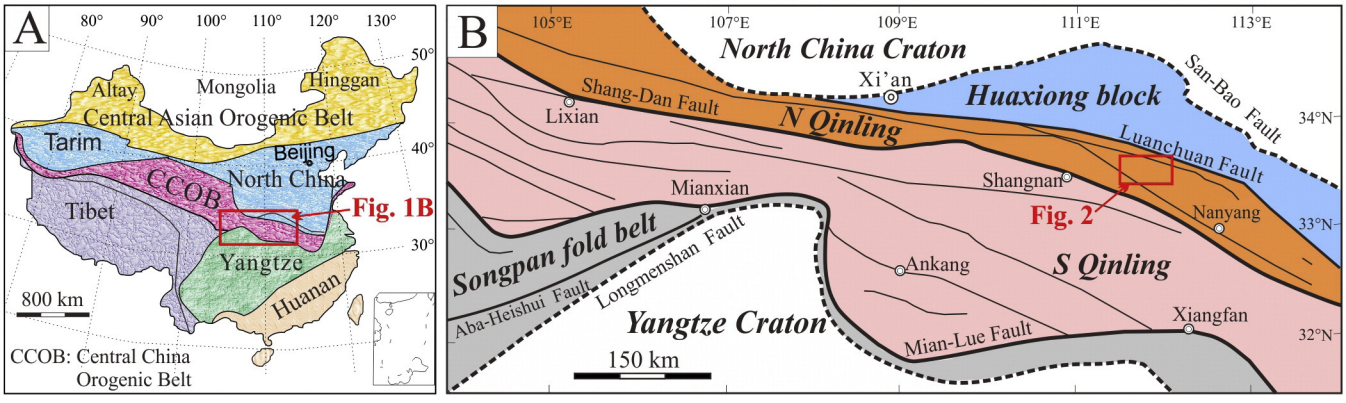

Fig. 1. (A) Tectonic subdivisions of China; (B) Tectonic subdivision of the Qinling Orogen, showing the location of the Xiaguan Ag–Pb–Zn field (modified after Zhang et al., 2014; Zhou et al., 2014).

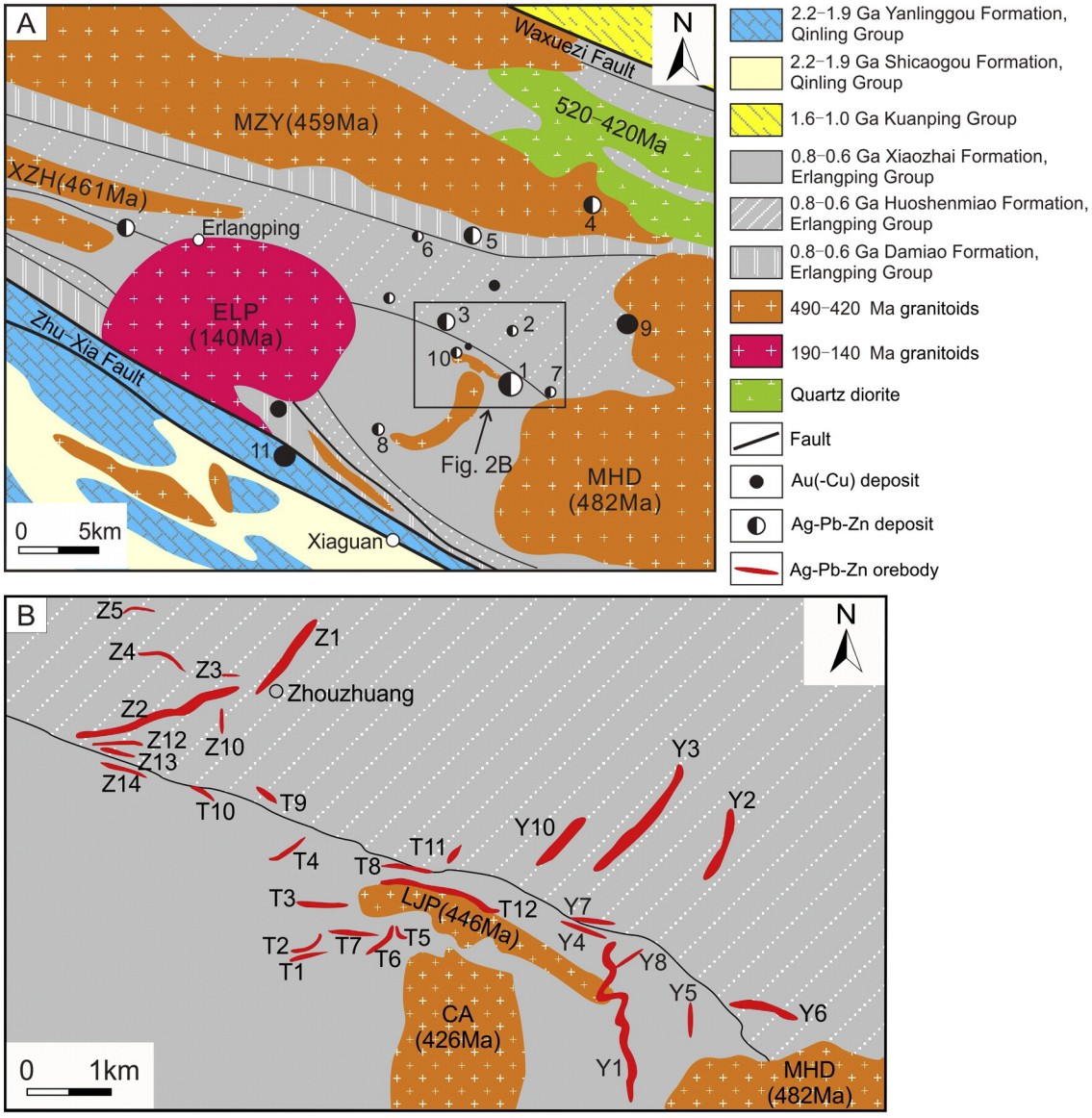

Fig. 2. (A) Geological map of the Xiaguan Ag–Au polymetallic orefield (modified after HINME, Henan Institute of Nonferrous Metal Exploration, 2003); (B) Distribution of the main Ag–Pb–Zn ore veins (modified after Zhang et al., 2004 and Cao et al., 2011). Granitic plutons: MHD, Muhuding granite pluton; ELP, Erlangping biotite monzonitic granite pluton; MZY, Manziying granite pluton; XZH, Xizhuanghe granodiorite pluton; LJP, Lujiaping granite pluton; CA, Cha'an granite pluton. Names of the deposits in Xiaguan area (numbered on the map): 1, Yindonggou; 2, Youhulugou; 3, Zhouzhuang; 4, Dongqinggou; 5, Shang'an; 6, Yinhuman; 7, Laozhuang; 8, Xiajiagou; 9, Xuyaogou; 10, Tumuya; 11, Banchang.

Orebodies are hosted by altered fractures, with thicknesses of quartz veins and alteration zones being 0.2–1.2 m and 10–30 m, respectively. The quartz-sulfide vein mineralization style is dominated at Xiaguan, and there is a distinct boundary between the orebodies and wallrocks. For example, in the Y1 (Yindonggou) and Z2 (Zhouzhuang) orebodies, quartz-sulfide-veins are found to crosscut the granite stock (Figs. 2B and 3A) and meta-gabbro, respectively (Figs. 2B and 3B).

Table 1
Occurrence characteristics and grades of main orebodies in Xiaguan Ag polymetallic orefield.

Deposit	Orebody	Length (m)	Thickness (m)	Occurrence	Ag (g/t)	Au (g/t)	Average Pb (%)	Average Zn (%)	Wallrock
Yindonggou	Y1	1800	0.5–1.7	270°–319° ∠ 16°–50°	80–446 (max 1234)	0.37–10.04	1.65	1.45	Sericite schist, granite
	Y2	1200	0.3–1.5	270°–310° ∠ 15°–38°	60–320	2.4–21.2	0.58	0.19	Spilite
	Y3	1600	0.8–1.4	260°–310° ∠ 36°–54°	70–235	1.6–2.1	7.37	3.31	Spilite
Zhouzhuang	Z1	900	0.5–1.6	130° ∠ 75°–84°	45–69	2.62	0.49	0.01	Spilite
	Z2	1200	0.8–1.5	114°–148° ∠ 54°–64°	5–687	0.20–2.78	1.76	1.24	Spilite, gabbro
Tumuya	T3	650	0.5–1.5	5°–15° ∠ 44°–64°	5–40	0.20–1.55			Sericite schist
	T6	600	0.3–0.6	310°–10° ∠ 10°–45°	40–400	3.48–14.56			Sericite schist
	T12	1200	0.5–4.0	20°–50° ∠ 50°	5–205	0.15–1.86			Altered rock

Note: Integrated after HINME (Henan Institute of Nonferrous Metal Exploration) (2003) and Wang et al. (2003).

Table 2
Microthermetric data of fluid inclusions (FIs) for the Xiaguan Ag–Pb–Zn orefield.

Stage	Hosted mineral	FIs Type	Number	$T_{m,CO2}$ (°C)	$T_{m,cla}$ (°C)	$T_{h,CO2}$ (°C)	$T_{m,ice}$ (°C)	T_h (°C)	Salinity (wt.% NaCl equiv.)	CO_2 density (g/cm^3)	Bulk density (g/cm^3)
Early	Quartz	C	47	−59.7 to −56.6	3.9–8.8	25.6–30.7		286–424(L)	2.4–10.7	0.58–0.71	0.93–1.01
	Quartz	C	10	−59.7 to −57.0	3.6–7.5	9.8–29.5		280–562(V)	4.8–11.1	0.63–0.87	0.87–0.99
	Quartz	C	7	−58.6 to −57.6	4.4–6.5	24.9–29.6		350–436(DP)	6.6–10.0	0.63–0.72	
	Quartz	PC	42	−58.6 to −57.6		21.6–30.1				0.61–0.75	
	Quartz	W	57				−11.4 to −0.2	158–416(L)	0.4–15.4		0.99–1.12
	Quartz	W	4				−12.1	320–362(V)	16.0		1.13
Middle	Quartz	C	5	−58.2 to −58.1	4.3–5.4	29.7–29.8		272–323(L)	8.5–10.1	0.62–0.63	0.88–0.95
	Quartz	C	4	−58.0 to −57.0	8.2–9.0	21.0–25.9		200–344(V)	2.0–3.6	0.71–0.77	0.84–0.85
	Quartz	C	18	−58.4 to −57.6	4.1–6.6	19.8–28.5		287–330(DP)	6.5–10.4	0.66–0.78	
	Quartz	PC	6			23.1–28.1				0.67–0.75	
	Quartz	W	104				−18.1 to −1.2	170–323(L)	2.1–21.0		1.01–1.17
Late	Quartz	C	2	−59.0 to −58.0	5.4–6.6	21.3–26.8		255–256(L)	6.5–8.4	0.69–0.77	0.94–0.97
	Quartz	C	3	−58.8 to −57.4	3.8–9.0	21.3–28.4		200–280(V)	2.0–10.9	0.68–0.88	0.86–0.91
	Quartz	W	20				−13.2 to −0.7	175–309(L)	1.2–17.1		1.00–1.13
	Calcite	W	18				−7.2 to −0.2	149–282(L)	0.4–10.7		0.99–1.08

Abbreviation: $T_{m,CO2}$ = melting temperature of solid CO_2; $T_{m,cla}$ = temperature of CO_2-clathrate dissociation; $T_{h,CO2}$ = homogenization temperature of CO_2; $T_{m,ice}$ = ice melting temperature; T_h = total homogenization temperature; L and V stand for liquid and vapor to which the fluid inclusions homogenize, respectively; DP means the temperature when FIs decrepitated before homogenization. The densities of CO_2 and bulk inclusions are estimated using the Flincor program (Brown, 1989) and the formula of Brown and Lamb (1989) for the H_2O–CO_2–NaCl system.

Y1 is the largest orebody at Yindonggou (ca. 1800 m long, 0.5–1.7 m thick and 390 m deep), and contains Ag grade of 80–446 g/t (locally reach 1234 g/t). Gold grade is 0.37–10.04 g/t, while the average Pb and Zn grades are 1.65% and 1.45%, respectively (Table 1).

3.2. Ore and mineral assemblages

The Ag ores at Xiaguan are hosted mainly by quartz-sulfide veins and minor by altered tectonites. For the quartz-sulfide vein type ores, the Ag-polymetallic ore minerals are disseminated in fine fracture-infilled veins (Fig. 4A), or occur as coarse-grain sulfide bands (Fig. 4B). In many places, sulfide minerals have infilled the fissures between cataclastic quartz (−chlorite) veins as scattered specks or thin veins (Fig. 4C). The altered tectonite ores usually occur along both sides of the quartz-sulfide veins.

Major metallic minerals include native Ag, argentite, tetrahedrite–freibergite, galena, sphalerite, pyrite, chalcopyrite and pyrargyrite (Fig. 4D–F), and major gangue minerals include quartz, sericite, chlorite and calcite (Fig. 4G–L). Silver mainly occurs in freibergite and Cu-bearing argentite, followed by in native Ag and pyrargyrite. These minerals are present mainly along the margins of galena and chalcopyrite or along the galena–sphalerite contacts (Fig. 4D–F). Silver and galena contents are strongly (positively) correlated, thus the galena-sphalerite-rich ores (Fig. 4B) have a richer Ag mineralization than the pyrite-rich ores (Fig. 4A, C).

3.3. Mineralization stage and wallrock alteration

Mineral deposits in the Xiaguan Ag–Pb–Zn orefield contain three paragenetic stages, i.e., the Early (E)-, Middle (M)-, and Late (L) stage, as identified by the hydrothermal mineral paragenesis, ore petrography and crosscutting relationships.

The E-, M- and L-stages are characterized by milky-white, pyrite/arsenopyrite-bearing coarse quartz-veins, polymetallic sulfide stockworks/bands and carbonate-quartz veinlets, respectively (Fig. 4A and B). Silver, Pb and Zn are enriched in M-stage ores, and poor in E- or

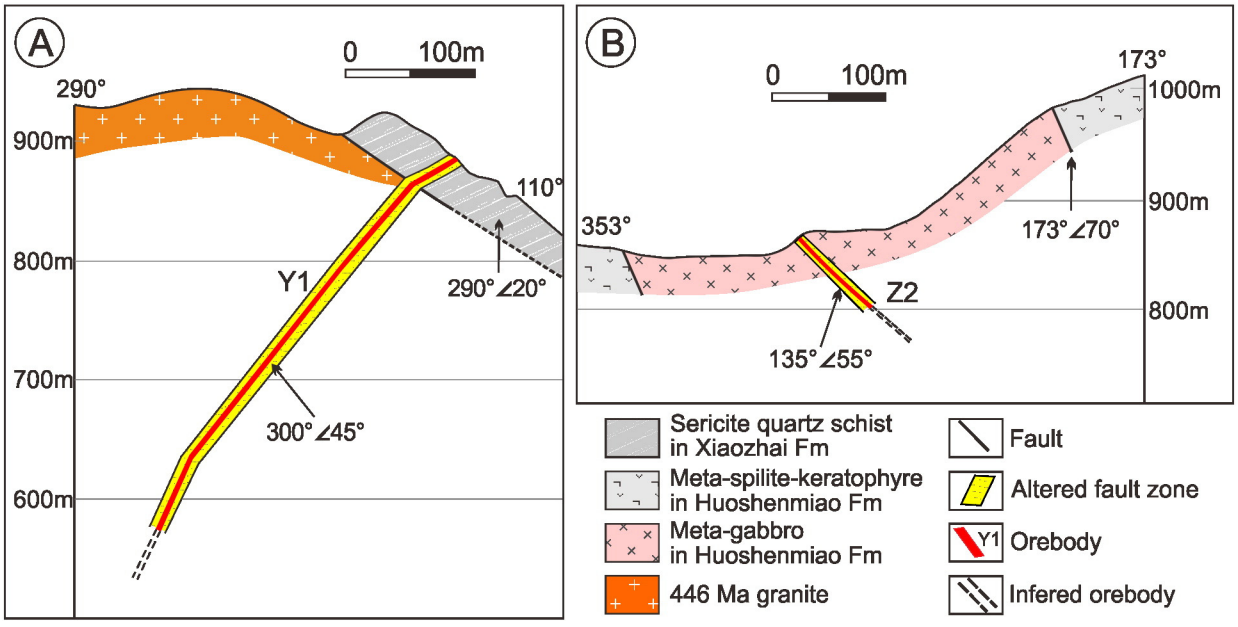

Fig. 3. Cross section of (A) No. 0 prospecting line at the Yindonggou deposit and (B) No. 1 prospecting line at the Zhouzhuang deposit (from HINME, Henan Institute of Nonferrous Metal Exploration, 2003).

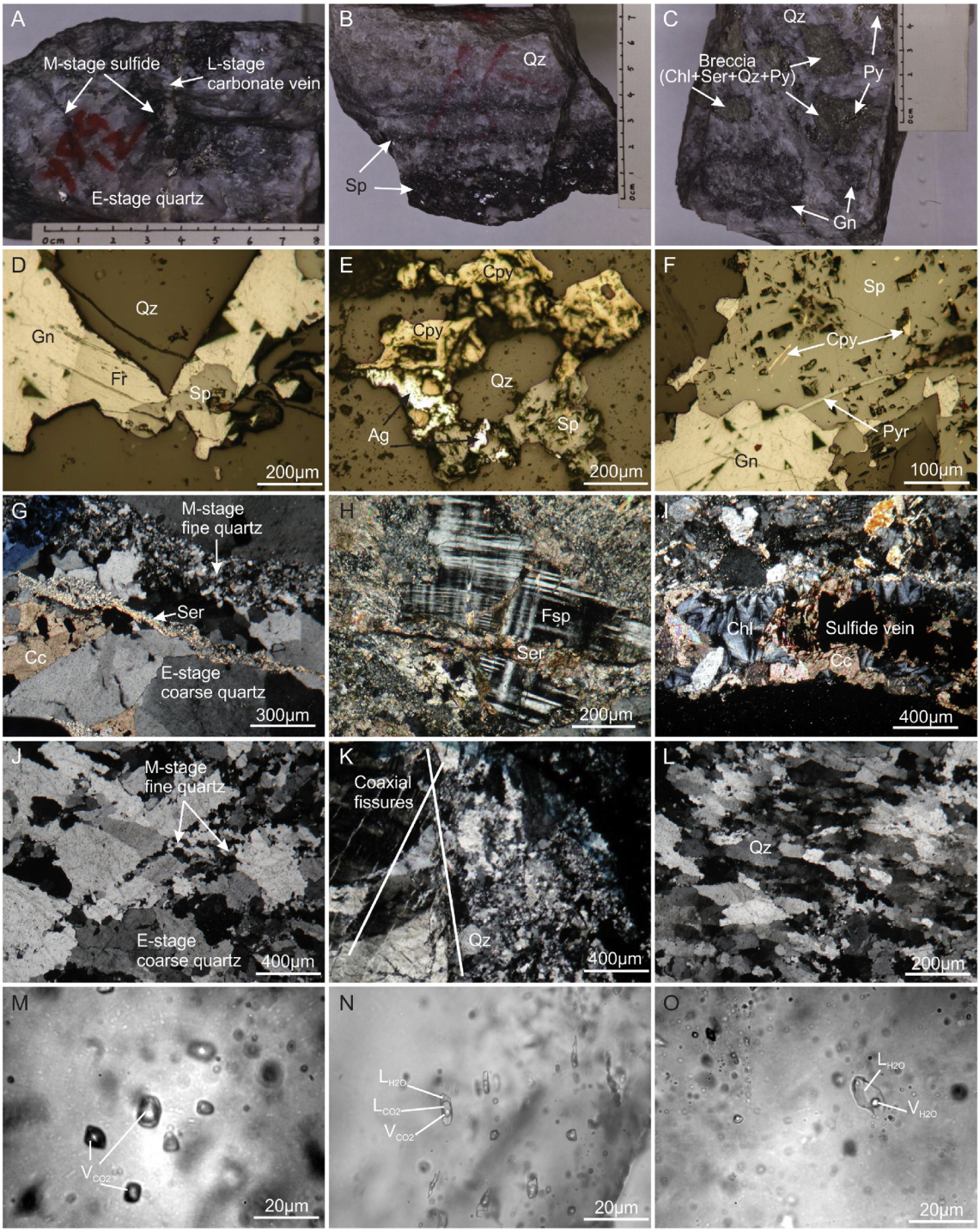

Fig. 4. Photos of ore petrography and FIs in the Xiaguan Ag–Pb–Zn orefield. A. E-stage quartz vein fractured and infilled by M-stage fine-grained quartz-sulfide stockworks, and then cut by L-stage carbonate veinlets; B. Banded Ag–Pb–Zn ore; C. Brecciated ore; D. Freibergite within galena (reflected light); E. Co-existing native silver, chalcopyrite and sphalerite (reflected light); F. Pyrargyrite cuts galena and sphalerite (reflected light); G. Sericitization and carbonation in a quartz-sulfide vein; H. Sericitization of feldspar in altered Lujiaping granite; I. Chlorite-calcite-sulfide vein; J. E-stage coarse-grained quartz cut by M-stage fine-grained quartz-sulfide stockworks (+); K. Co-axial joints within E-stage quartz (+); L. Wavy extinction texture of E-stage quartz; M. PC-type FIs in E-stage quartz; N. C-type FI cluster in M-stage quartz; O. W-type FIs in L-stage quartz. Abbreviation: Qz, quartz; Py, pyrite; Gn, galena; Sp, sphalerite; Fr, freibergite; Cpy, chalcopyrite; Ag, native silver; Pyr, pyrargyrite; Cc, calcite; Ser, sericite; Fsp, feldspar; Chl, chlorite; V_{CO2}, vapor CO_2; L_{CO2}, liquid CO_2; V_{H2O}, vapor water; L_{H2O}, liquid water.

L-stage ones, indicating that M-stage is the main mineralization phase, a common feature for orogenic-type deposits (Hagemann and Luders, 2003; Chen et al., 2004, 2005; Jiang et al., 2009; Chen et al., 2012; Deng et al., 2014b).

E-stage quartz and pyrite crystals were deformed and broken, and were replaced and/or filled by M- and/or L-stage minerals (Fig. 4A, J–L), indicating compressive or shearing tectonics. M-stage polymetallic sulfide stockworks have usually filled crevices, and are locally co-axial (Fig. 4J and K) with E-stage quartz veins or altered wallrocks. M-stage samples are not deformed or brecciated, suggesting a tectonic setting of relaxation. Comb texture characterizes L-stage quartz/calcite veinlets (Fig. 4I), demonstrating extensional tectonics during this stage.

Hydrothermal alteration associated with the Xiaguan Ag polymetallic mineralization includes silicic-, sericite-, pyrite-phyllic-, carbonate and

chlorite alteration, which is similar to typical vein-hosted Au deposits, such as the Wenyu deposit in the Xiaoqinling orefield in China (Zhou et al., 2014).

4. Analytical methods

Microthermometric measurements were performed at the Fluid Inclusion (FI) Laboratory of the Institute of Geology and Geophysics, Chinese Academy of Science, using the Linkam THMSG600 heating-freezing stage and standard procedures. Stage calibration was carried out at −56.6 °C, −10.7 °C and 0.0 °C using synthetic FIs supplied by FLUID INC. The measurement precisions are estimated to be ±0.2 °C for <30 °C, ±1 °C for the interval of 30−300 °C, and ±2 °C for >300 °C. Melting temperatures of solid CO_2 ($T_{m,CO2}$), freezing point of NaCl-H_2O inclusions ($T_{m,ice}$), final melting temperatures of clathrate ($T_{m,cla}$), homogenization temperatures of vapor CO_2 + liquid CO_2 ($T_{h,CO2}$) and total homogenization temperatures of FIs (T_h) were measured. Heating rate was 1−5 °C/min during the initial stages of each heating run and reduced to 0.3−1 °C/min close to the phase change points. Salinities of carbonic (CO_2–H_2O) and aqueous (NaCl–H_2O) inclusions were calculated using the final melting temperatures of CO_2–clathrate (Collins, 1979) and ice points (Bodnar, 1993), respectively.

Composition of individual FI was obtained using a RW-1000 Laser Raman spectroscopy at the State Key Laboratory of Orogen and Crust Evolution, Peking University. An argon laser with wavelength of 514.5 nm was used as laser source at power of 1000 mW. The spectral range falls between 500 and 4000 cm^{-1} for the analysis of H_2O, CO_2, CH_4, and N_2 in the vapor and liquid phases. Integration time was 10 s, with 10 accumulations for each spectral line. The spectral resolution was ±20 mm^{-1} with a beam size of 2 μm.

Samples used for isotope analyses were selected from the specimens by optical microscopy to confirm the mineralization stage they represent. Aggregates of quartz and sulfides were separated from the specimens using pincers and were then crushed into grains with size of 40–60 mesh. After panning and filtration, more than 10 g of clear mineral grains was picked out for each sample under binocular microscope. In order to eliminate other interlocking minerals (e.g., sulfides), quartz separates were soaked in HNO_3^- solution at 60–80 °C for 12 h and rinsed by deionized water. The separates were treated six times using supersonic centrifugal filter and rinsed by deionized water over a week. The samples were dried in an oven at 120 °C before analysis. For sulfides, approximately 10 to 50 mg were first leached in acetone to remove surface contamination and then washed by distilled water and dried at 60 °C in the oven.

The oxygen and carbon isotopes were analyzed on a Finnigan MAT252 mass spectrometer and the hydrogen isotope on MAT253 in the State Key Laboratory of Lithosphere Evolution, Institute of Geology and Geophysics, Chinese Academy of Science. Oxygen gas was generated from the samples by quantitatively reaction with BrF_5 in externally heated nickel vessels. Hydrogen in the extracted water from the FIs in quartz separates was replaced by Zn and released for mass spectrometry. Carbon was measured on CO_2, which was liberated from Fis in quartz separates by thermal decrepitation under vacuum. The isotope data were reported in per mil relative to the Vienna SMOW standard for oxygen and hydrogen, and to the Peedee Belemnite (PDB) standard for carbon. Total uncertainties were estimated to be better than ±0.2 ‰ for $\delta^{18}O$, ±2.0 ‰ for δD and ±0.2 ‰ for $\delta^{13}C$.

Sulfur isotope ratios of sulfides were analyzed on SO_2 using Delta-S mass spectrometer, and the Pb isotopic compositions were measured on MAT-261 Thermal Ionization Mass Spectrometer (TIMS) with the standard sample NBS 981 at the Open Laboratory of Isotopic Geochemistry, Chinese Academy of Geological Sciences. Washed sulfides were dissolved in dilute mix solution of nitric acid and hydrofluoric acid. Following ion exchange chemistry, the Pb in the solution was loaded onto Re filaments using a phosphoric acid-silica gel emitter. The S-isotopic compositions were reported relative to the Canyon Diablo Triolite (CDT) standard. Total uncertainties were estimated to be better than ±0.2 ‰ for $\delta^{34}S$ at the σ level and the estimated precision for $^{206}Pb/^{204}Pb$, $^{207}Pb/^{204}Pb$ and $^{208}Pb/^{204}Pb$ ratios are about 0.1%, 0.09% and 0.30% at the 2σ level, respectively.

The $^{40}Ar/^{39}Ar$ plateau age was analyzed at the Geochronology Research Laboratory of Queen's University, Ontario, Canada. $^{40}Ar/^{39}Ar$ analyses were performed by standard laser step-heating techniques described in detail by Clark et al. (1998). All data have been corrected for blanks, mass discrimination, and neutron-induced interferences. A plateau age was obtained when the apparent ages of at least three consecutive steps, comprising a minimum of 55% of the $^{39}Ar_k$ released, agree within 2σ error with the integrated age of the plateau segment. Errors and isotope-correlation diagrams represent the analytical precision at ±2σ.

5. Ore-forming fluid system

5.1. Types and populations of the FIs

Three FI types are identified based on their phases at room- (ca. 21 °C) and subzero temperatures, phase transitions during heating and cooling runs (−196 to +600 °C), and Laser Raman spectroscopy. These three FI types are namely: pure CO_2 (PC-type), CO_2-H_2O (C-type) and aqueous (W-type). The PC-type FIs appear as monophase (liquid CO_2) or two-phase (liquid CO_2 + vapor CO_2) inclusions at room temperature (Fig. 4M), commonly coexisting with C-type FIs. They are irregular, ellipsoidal and negative quartz crystal in shapes, with sizes of 10–20 μm. The C-type FIs consist of two (liquid CO_2 + liquid H_2O) or three phases (vapor CO_2 + liquid CO_2 + liquid H_2O), with the CO_2 phase accounting for 20−80 vol.% (Figs. 4N and 5). They appear as irregular, ellipsoidal and negative quartz crystal in shape, 10–20 μm in size, and occur as isolated FIs or in clusters. The W-type FIs usually appear as two-phase (liquid H_2O and vapor H_2O) NaCl-H_2O systems (Fig. 4O), with vapor bubbles accounting for 5−60 vol.%. They are irregular, ellipsoidal, strip and negative crystal in shape, with sizes of 5–20 μm.

Relative abundance of the three FI types was investigated for each sample of different stages and depths. Both E- and M-stage quartz contains all the three FI types, with PC- and C-type FIs predominate. In L-stage minerals, W-type FIs dominate together with minor C-type FIs. C-type FIs decreases from E- to L-stage and from deep (760 m) to shallow (910 m) level. On the contrary, W-type FIs increase from E- to L-stage and from deep to shallow level. All these variations indicate that the hydrothermal fluids had changed from carbonic to aqueous with time and upward migration.

5.2. Microthermometry of the FIs

In the E-stage quartz, the FIs are mainly of C- and PC-type, with minor W-type FIs. The melting temperatures of solid CO_2 ($T_{m,CO2}$) in C-type FIs range from −59.7 to −56.6 °C (Table 2), slightly below the triple-phase point of pure CO_2 (−56.6 °C), suggesting minor amounts of dissolved components in the carbonic phase, such as methane. The melting temperatures of clathrate ($T_{m,cla}$) are between 3.6 and 8.8 °C, corresponding with salinities of 2.4 to 11.1 wt.% NaCl equiv. The FIs are totally homogenized to liquid or vapor at temperatures (T_h) between 280 and 562 °C, clustering around 300−370 °C (Table 2, Fig. 6), with carbonic phases being homogenized to vapor or liquid temperatures ($T_{h,CO2}$) of 9.8–30.7 °C; but some C-type FIs with high V/L (vapor/liquid) ratios (>50%) are decrepitated at temperatures of 350–436 °C prior to final homogenization due to high inner pressure (Table 2). The calculated CO_2 densities range from 0.58 to 0.87 g/cm^3 and bulk densities from 0.87 to 1.01 g/cm^3. The two phase PC-type FIs yield $T_{m,CO2}$ values of −58.6 to −57.6 °C and homogenization (to liquid) temperatures of CO_2 ($T_{h,CO2}$) of 21.6 to 30.1 °C, corresponding to densities of 0.61 to 0.75 g/cm^3. The W-type FIs yielded ice-melting

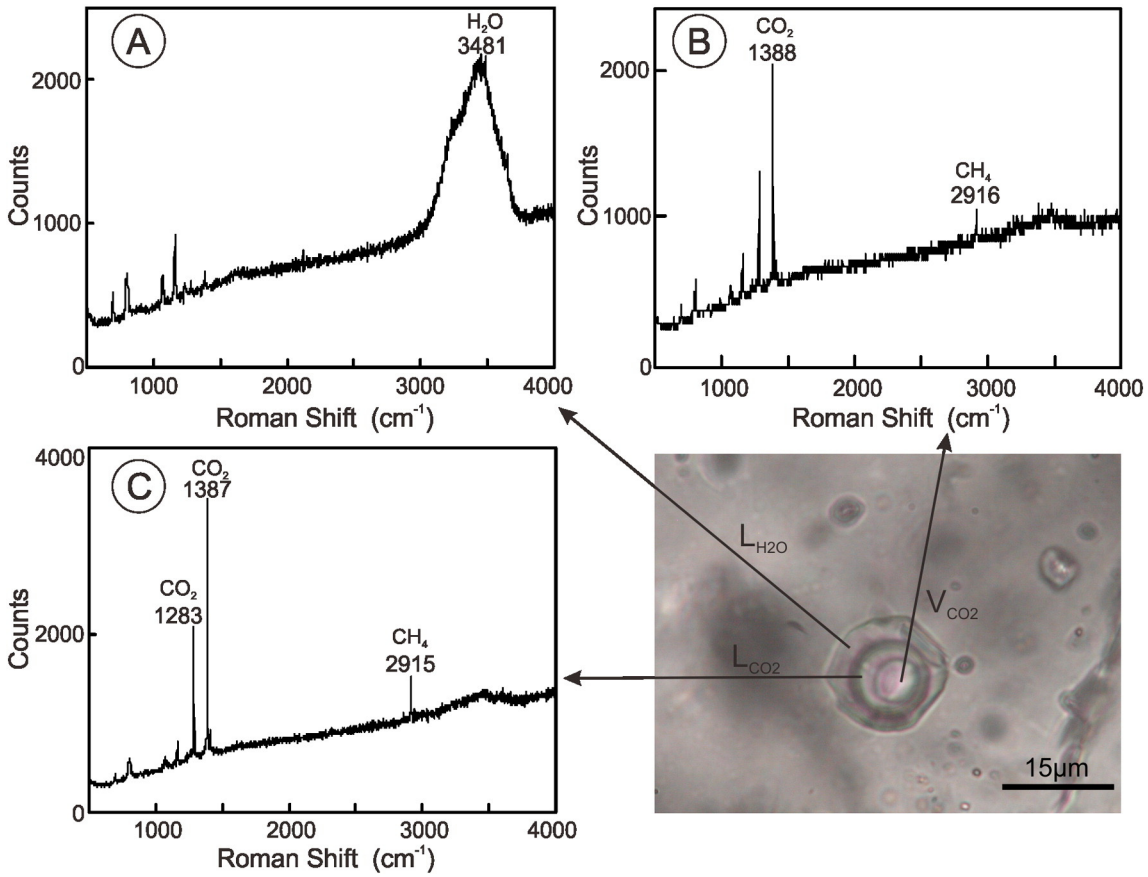

Fig. 5. Laser Roman spectra of the CO_2-bearing FIs in M-stage quartz.

temperatures ($T_{m,ice}$) at −12.1 to −0.2 °C, with salinities ranging from 0.4 to 16.0 wt.% NaCl equiv. They homogenized to liquid at temperatures of 158−416 °C, with solution densities of 0.99−1.13 g/cm^3.

The main-stage quartz contains all the three FIs types identified at Yindonggou and Zhouzhuang deposits (Table 2). For the C-type FIs, the $T_{m,CO2}$ values of range from −58.4 to −57.0 °C, the CO_2 clathrate ($T_{m,cla}$) is melted at the temperature of 4.1 to 9.0 °C, corresponding to salinities of 2.0−10.4 wt.% NaCl equiv., and the CO_2 phases are generally homogenized to liquid at 19.8–29.8 °C ($T_{h,CO2}$). These low $T_{m,CO2}$ (<−56.6 °C) and $T_{h,CO2}$ (<31.1 °C) values indicate that the CO_2 phase contains a small, but variable amount of CH_4 and/or N_2, which has been confirmed by laser Raman spectroscopy (Fig. 5). They are totally homogenized to liquid at 272–323 °C, or to vapor at 200–344 °C, but many decrepitated at temperatures of 287–330 °C prior to total homogenization due to high inner pressure. The C-type FIs yield bulk densities of 0.84 to 0.95 g/cm^3, and CO_2 densities of 0.62 to 0.78 g/cm^3. The PC-type FIs show two phases and the $T_{h,CO2}$ values vary from 23.1 to 28.1 °C, corresponding to densities of 0.67 to 0.75 g/cm^3. These data also imply for a remarkable content of other gases such as CH_4. The W-type FIs are usually observed in the vicinity of PC- and C-type FIs. Their freezing point depression varies from −18.1 to −1.2 °C, with estimated salinities of 2.1−21.0 wt.% NaCl equiv. and solution densities of 1.01−1.17 g/cm^3. They are homogenized to liquid at temperatures of 170−323 °C.

The fluid inclusions in L-stage quartz and calcite are mainly of W-type, and minor of C-type. The W-type FIs yield $T_{m,ice}$ of −13.2 to −0.2 °C, salinities of 0.4−17.1 wt.% NaCl equiv., and homogenization (to liquid) temperature of 149 °C to 309 °C, with solution densities ranging from 0.99 to 1.13 g/cm^3. The minor C-type FIs yield $T_{m,CO2}$ of −59.9−−58.0 °C, and $T_{m,cla}$ of 3.8−9.0 °C, corresponding to salinities of 2.0−10.9 wt.% NaCl equiv. The CO_2 phases are generally homogenized to liquid at 21.3–28.4 °C and the total homogenization temperatures range from 200 °C to 280 °C.

5.3. Trapping pressure of FIs and mineralization depth

The C-type fluid inclusions are common in E- and M- stages, and minor in L-stage at Yindonggou deposit. Therefore, the pressure was estimated based on the CO_2–H_2O–NaCl system, using the Flincor program (Brown, 1989) and the formula of Brown and Lamb (1989). The minimum trapping pressures of FIs were estimated to be ca. 280–320 MPa in E-stage, ca. 250−277 MPa in M-stage, and ca. 90–92 MPa in L-stage, with total homogenization temperatures ranging from 281 to 344 °C, 308–343 °C to 200–280 °C respectively (Table 3). According to the estimated trapping pressures, we conclude that E-stage mineralization at Yindonggou was likely to have formed at a depth of ca. 10.2–11.7 km, M-stage at ca. 9.1–10.1 km and L-stage at ca. 3.3–3.4 km deep (L-stage hydrostatic depth: ca. 9.2–9.4 km), which is consistent with the depth of the Zhouzhuang deposit (Table 3; Cao et al., 2011).

The estimations above show that the trapping pressures of FIs and mineralization depth gradually decreased from early through middle to late stages, which is common in orogenic deposits and could be promoted by the uplifting- or exhumation-related seismicity (Sibson et al., 1988; Zheng et al., 2012; Zhang et al., 2012, 2013; Deng et al., 2014b). Besides, secondary FIs (with salinity of 1.7 wt.% NaCl equiv. and density of 0.93 g/cm^3) are of W-type and with calculated capture pressure of ca. 0.6 MPa, corresponding to a hydrostatic depth of about 600 m. This suggests that the post-ore meteoric water circulation occurred at very shallow depths.

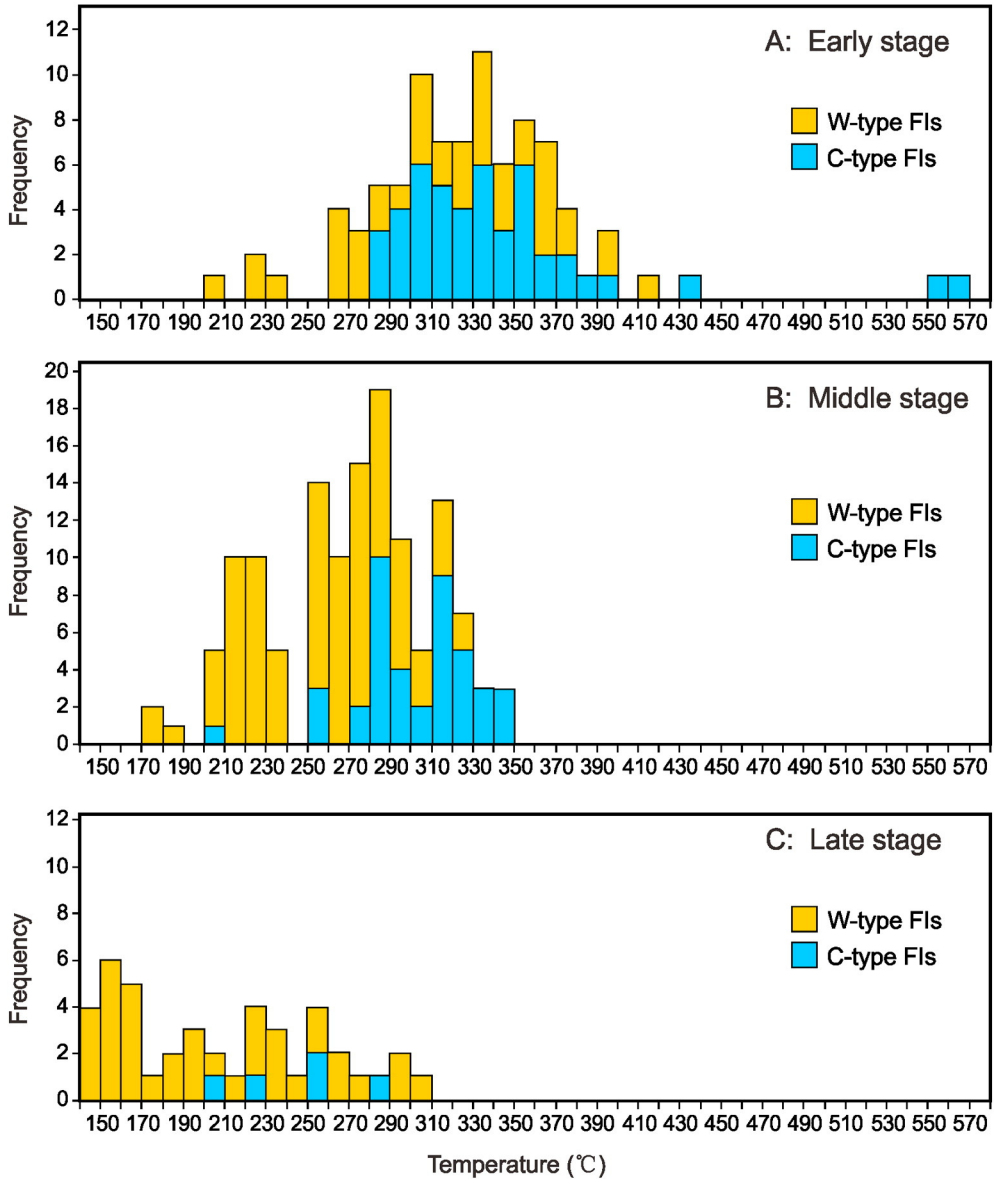

Fig. 6. Histograms for temperatures of FIs in Xiaguan Ag–Pb–Zn orefield.

6. Isotope geochemistry and geochronology

6.1. Hydrogen-oxygen isotope

The analytical data on oxygen and hydrogen isotopes of quartz, and calculated $\delta^{18}O_{water}$ values of the Xiaguan ore-forming fluids are listed in Table 4. At Yindonggou, fluids of E-stage quartz have $\delta^{18}O_{water}$ values of 7.8–10.8 ‰ and δD values of −95 – −46 ‰. The $\delta^{18}O$ values of the M-stage fluids are 6.4–9.4 ‰ and the δD values are between −82 ‰ and −73 ‰. The $\delta^{18}O_{water}$ values of L-stage quartz are 3.1–3.3 ‰ and δD values are between −95 ‰ and −82 ‰, and $\delta^{18}O_{water}$ values of L-stage calcite vary from −1.6 ‰ to 0.4 ‰.

At Zhouzhuang, calculated $\delta^{18}O_{water}$ values of the FIs decrease progressively from E-stage (8.6–9.9 ‰), through M-stage (6.0–6.5 ‰) to

Table 3
Microthermometric result for different stage FIs at Xiaguan Ag–Pb–Zn orefield.

Deposit stage	Sample no.	FI type	Number	T_h (°C)	Salinity (wt.% NaCl equiv.)	Pressure (MPa)	Depth (km)	Ref.
Yindonggou								
Early	YDG-13	C	8	281–344	7.3–9.7	280–320	10.2–11.7	This paper
Middle	YDG-15	C	8	308–343	4.9–9.1	250–277	9.1–10.1	This paper
Late	YDG-17	C	3	200–280	2.0–10.9	90–92	3.3–3.4(9.2 − 9.4)	This paper
Zhouzhuang								
Early	–	C	–	270–310	6–10	235–270	8.6–9.8	Cao et al. (2011)
Middle	–	C	–	200–230	14–18	200–230	7.3–8.4	Cao et al. (2011)
Late	–	W	–	150–180	8–12	39–79	1.4–2.9(4.0 − 8.1)	Cao et al. (2011)

Note: The depths are estimated as lithostatic pressure, given the rock density to be 2.8 t/m^3; and the depths in brackets for late stage are estimated as hydrostatic pressure. The other abbreviations and notations are the same in Table 2.

Table 4
$\delta^{18}O$, δD and $\delta^{13}C$ values (‰) of the Xiaguan Ag–Pb–Zn orefield.

Sample	Mineral	Stage	$\delta^{18}O_{mineral}$	$\delta^{18}O^{(a)}_{H2O}$	δD_{H2O}	$\delta^{13}C_{mineral}$	$\delta^{13}C^{(b)}_{CO2}$	T (°C)	Reference
Yindonggou deposit									
YDG-3	Quartz	Early	12.1	8.4	−95		0.1	416	This study
YDG-41	Quartz	Early	12.2	8.5	−83		0.2	416	This study
YDG-42	Quartz	Early	13.0	9.3	−46		0.3	416	This study
YDG-2	Quartz	Early	11.5	7.8				416	This study
YDG-13	Quartz	Early	14.5	10.8	−80		0.1	416	This study
YDG-31	Quartz	Middle	14.5	8.4	−78		0.2	323	This study
YDG-32	Quartz	Middle	12.5	6.4	−73		0.4	323	This study
YDG-12	Quartz	Middle	14.7	8.6				323	This study
YDG-14	Quartz	Middle	15.5	9.4	−82		0.9	323	This study
YDG-15	Quartz	Middle	13.1	7.0				323	This study
YDG-16	Quartz	Middle	14.2	8.1				323	This study
YDG-3A	Quartz	Late	12.1	3.1	−95		0.1	248	This study
YDG-17	Quartz	Late	12.3	3.3	−82		−0.2	248	This study
	Calcite	Late	10.0	−1.6		−2.2	−3.5	165	Cao et al. (2011)
	Calcite	Late	11.5	−0.1		−2.4	−3.7	165	Cao et al. (2011)
	Calcite	Late	12.0	0.4		−5.5	−6.8	165	Cao et al. (2011)
Zhouzhuang deposit									
	Quartz	Early	13.6	9.9	−70			416	Cao et al. (2011)
	Quartz	Early	13.1	9.4	−59			416	Cao et al. (2011)
	Quartz	Early	12.3	8.6	−65			416	Cao et al. (2011)
	Quartz	Middle	12.5	6.4	−80			323	Cao et al. (2011)
	Quartz	Middle	12.1	6.0	−82			323	Cao et al. (2011)
	Quartz	Middle	12.6	6.5	−70			323	Cao et al. (2011)
	Calcite	Late	11.1	−0.5	−90	−3.3	−4.6	165	Cao et al. (2011)
	Calcite	Late	10.6	−1.0		−3.4	−4.7	165	Cao et al. (2011)
	Calcite	Late	10.1	−1.5		−3.9	−5.2	165	Cao et al. (2011)

Notes: The temperatures used in calculation are the peak values of fluid inclusion homogenization temperatures for individual samples or mineralization stages. (a) The $\delta^{18}O_{H2O}$ of ore fluids in equilibrium with quartz or calcite is calculated using equations of $1000\ln\alpha_{quartz\text{-}water} = 3.38 \times 10^6\, T^{-2} - 3.40$ (Clayton et al., 1972) and $1000\ln\alpha_{calcite\text{-}water} = 2.78 \times 10^6\, T^{-2} - 2.89$ (Zhang, 1989). (b) The $\delta^{13}C_{CO2}$ values refer to CO_2 released from fluid inclusions. The $\delta^{13}C_{CO2}$ ratios of calcites were calculated using $1000\ln\alpha_{calcite-CO2} = -0.388 \times 10^9 / T^3 + 5.538 \times 10^6 / T^2 - 11.346 \times 10^3 / T + 2.962$ (0–3000 °C) (Chacko et al., 1991).

L-stage (−1.5 – −0.5 ‰), with corresponding δD values being −70 to −65 ‰, −82 to −70 ‰ and −90 ‰, respectively (Cao et al., 2011). The data point distributions and trends are similar to those of the Yindonggou deposit, which altogether reflect the general Xiaguan ore-forming fluid characteristics (Fig. 7).

6.2. Carbon isotope

The $\delta^{13}C_{CO2}$ values of the ore-forming fluids in the E- and M-stage quartz at Yindonggou vary between 0.1 ‰ and 0.9 ‰, with an average of 0.3 ‰ (Table 4). The $\delta^{13}C_{CO2}$ values of the FIs in the Yindonggou L-stage quartz are −0.2–0.1 ‰, while those in the L-stage calcite at Yindonggou and Zhouzhuang range from −6.8 ‰ to −3.5 ‰ (Table 4). The L-stage $\delta^{13}C_{CO2}$ values are lower than those of E- and M-stage.

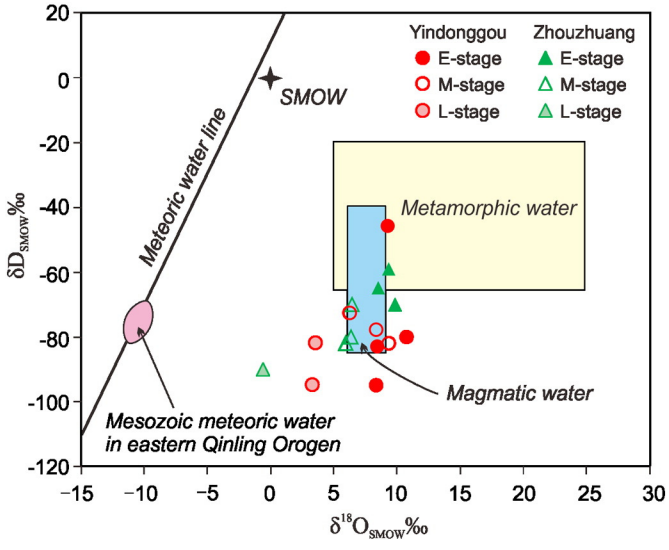

Fig. 7. Plot of δD vs. $\delta^{18}O$ of the ore-forming fluids in the Xiaguan Ag–Pb–Zn orefield. The base map is from Taylor (1974), domain of the Mesozoic meteoric water in the eastern Qinling Orogen is from Zhang (1989) and FI data are listed in Table 4.

6.3. Sulfur isotope

Sulfur isotope analyses were performed on sulfide samples from different ore types at Xiaguan, which fall in the range of 1.9 – 8.1 ‰ (Table 5, Fig. 8). Four pyrite samples have high $\delta^{34}S$ values of 5.9–8.1 ‰ (Avg. 7.3 ‰); 15 sphalerite samples yield $\delta^{34}S$ values of 3.1–7.1 ‰ (Avg. 6.0 ‰); and the $\delta^{34}S$ values of seven galena samples vary between 1.8 ‰ and 5.7 ‰ (Avg. 3.9 ‰). In the Y1 orebody, the $\delta^{34}S$ values decrease gradually from the coexisting pyrite to sphalerite or galena, indicating equilibrium fractionation of sulfur isotope between the major sulfides (Hoefs, 2004).

6.4. Lead isotope

Sulfides from Xiaguan have $^{206}Pb/^{204}Pb$, $^{207}Pb/^{204}Pb$, and $^{208}Pb/^{204}Pb$ values of 18.202–18.446 (Avg. 18.307), 15.567–15.773 (Avg. 15.634) and 38.491–39.089 (Avg. 38.655), respectively. The Erlangping Group spilite, keratophyre and schist have $^{206}Pb/^{204}Pb$, $^{207}Pb/^{204}Pb$, and $^{208}Pb/^{204}Pb$ values of 17.769–18.669 (Avg. 18.234), 15.494–15.807 (Avg. 15.615) and 38.284–39.130 (Avg. 38.630), respectively. The Qinling Group marble, gneiss and amphibolite have $^{206}Pb/^{204}Pb$, $^{207}Pb/^{204}Pb$, and $^{208}Pb/^{204}Pb$ values of 17.494–18.608 (Avg. 18.132), 15.405–15.636 (Avg. 15.550), and 37.378–39.418 (Avg. 38.286), respectively (Table 6). When compared to the volcanic-sedimentary strata and granitoids in eastern Qinling Orogen, all sulfides have narrow ranges of $^{206}Pb/^{204}Pb$ and $^{207}Pb/^{204}Pb$ and show an approximate linear distribution in Fig. 9.

Table 5
Sulfur isotopic data for the Xiaguan Ag–Pb–Zn orefield (‰).

Deposit orebody	Sample	Mineral	$\delta^{34}S$	Reference
Yindonggou				
Y1	YDG-30	Pyrite	7.6	This paper
	YDG-32	Pyrite	5.9	This paper
	YDG-3	Pyrite	8.1	This paper
	YDG-4	Pyrite	7.6	This paper
	YDG-15	Sphalerite	6.9	This paper
	YDG-16	Sphalerite	7.0	This paper
	YDG-12	Sphalerite	6.2	This paper
	YT-13	Sphalerite	7.3	Xiang et al. (2012)
	YT-24	Sphalerite	6.5	Xiang et al. (2012)
	YT-34	Sphalerite	6.9	Xiang et al. (2012)
	YDG-30	Galena	4.7	This paper
	YDG-32	Galena	4.8	This paper
	YDG-12	Galena	5.3	This paper
	YDG-4	Galena	5.7	This paper
Youhulugou				
Y3	YT3-2	Sphalerite	5.9	Xiang et al. (2012)
	YT3-4	Sphalerite	5.8	Xiang et al. (2012)
	YT3-7	Sphalerite	6.6	Xiang et al. (2012)
Y10	YT10-3	Galena	2.5	Xiang et al. (2012)
	YT10-4	Galena	2.4	Xiang et al. (2012)
	YT10-6	Galena	1.9	Xiang et al. (2012)
Laozhuang				
Y6	YT-45	Sphalerite	7.1	Xiang et al. (2012)
	YT-46	Sphalerite	7.3	Xiang et al. (2012)
	YT-51	Sphalerite	6.6	Xiang et al. (2012)
Zhouzhuang				
Z2	Z2-1	Sphalerite	3.2	Xiang et al. (2012)
	Z2-4	Sphalerite	3.3	Xiang et al. (2012)
	Z2-11	Sphalerite	4.3	Xiang et al. (2012)

6.5. $^{40}Ar/^{39}Ar$ isotope dating

Step heating $^{40}Ar/^{39}Ar$ dating on sericite from the altered tectonites at Yindonggou Ag–Pb–Zn deposit was conducted to constrain the metallogenic ages. The results show a stair-shaped spectrum (Fig. 10A), yielding individual step $^{40}Ar/^{39}Ar$ ages of 85.62 ± 20.06 Ma to 225.72 ± 3.56 Ma (Table 7). Although these data cannot form the Ar–Ar isochron or reverse isochron, the ratios of Cl/K, Ca/K and the figure of Ar (atmos Ar) vs. ^{39}Ar (Fig. 10B) show that the sample has high purity, and the data tested are trustworthy. Considering that sericite crystallization occurred during a multistage cooling, low-temperature and long hydrothermal process, we propose that the stair-shaped spectrum has recorded the sericite formation, and infer that: (1) ^{39}Ar loss was caused by later hydrothermal process; (2) Multistage mineralization probably occurred at Yindonggou, and has eventually ended no later than 85.62 ± 20.06 Ma; and (3) Four central consecutive steps, comprising >50% of the $^{39}Ar_k$ released (Table 7), give $^{40}Ar/^{39}Ar$ ages of 124.56 ± 1.56 Ma, 160.97 ± 1.06 Ma, 179.71 ± 2.03 Ma and 187.81 ± 2.08 Ma, respectively, suggesting that the sericite was mainly crystallized during ca. 187 − 124 Ma, consistent with the ages of the Songduo granitoid (ca. 190–140 Ma, Wang et al., 2003).

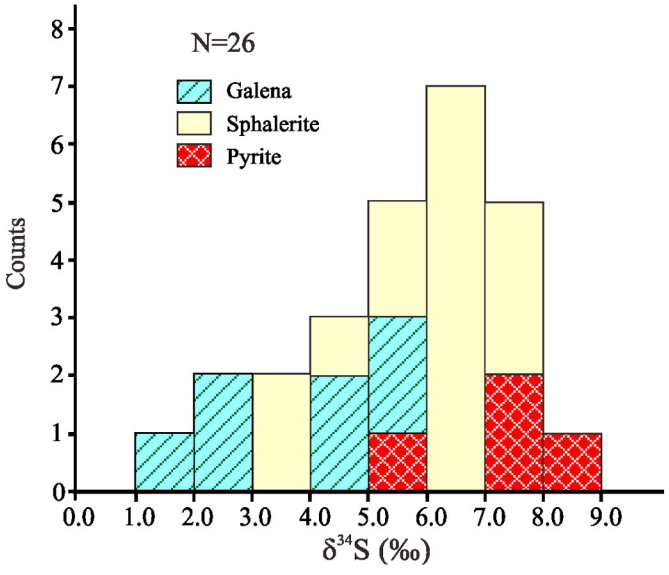

Fig. 8. Histogram of S-isotope of ore sulfides.

7. Discussion

7.1. Origin and evolution of ore-fluid system

The E- and M-stage H–O isotopic data are distributed within or under the fields of metamorphic water and magmatic water (Fig. 7). The L-stage H–O isotopic data points trend toward the meteoric water line, especially toward the domain of Mesozoic meteoric water in the Qinling Orogen (Fig. 7), drawn from H–O isotope studies of many Mesozoic meteoric hydrothermal deposits there (Zhang, 1989). This shows that the L-stage ore-forming fluids were either of meteoric origin or had been extensively mixed with meteoric water.

The $\delta^{13}C_{CO2}$ values (0.1 ‰ to 0.9 ‰) of the ore-forming fluids in E- and M-stage quartz are higher than those of organic matter (ca. −27 ‰), atmospheric CO_2 (−7 to −11 ‰; Hoefs, 2004), freshwater carbonate (−9 to −20 ‰; Hoefs, 2004), igneous rocks (−3 to −30 ‰; Hoefs, 2004), continental crust (−7 ‰; Faure, 1986) and the mantle (−5 to −7 ‰; Hoefs, 2004). Therefore, CO_2 in the Xiaguan fluid system was unlikely to be supplied by any one (or a mixture) of the above-mentioned carbon reservoirs. Marine carbonates, which have the highest $\delta^{13}C$ value (ca. 0.5 ‰; Schidlowski, 1998), represent a possible candidate, or at least as an end-member of the source should fluid mixing had occurred. At Xiaguan, carbonates of the Qinling Group may have contributed the CO_2 needed for the ore-forming system via metamorphic decarbonation, especially at the E- and M-stages. The L-stage $\delta^{13}C_{CO2}$ values (−6.8 ‰ to −3.5 ‰) are lower than those of E- and M-stage, suggesting that the L-stage fluid system may have contained a significant meteoric water component, which efficiently reduced the $\delta^{13}C$ value.

Fluid boiling can be inferred to have occurred at Yindonggou, as evidenced by: (1) Three different FI types coexist in the M-stage quartz (e.g., YDG15); (2) The coexisting vapor- and liquid-rich W-type FIs have similar homogenization temperature of 320–343 °C to gas phase, and 291–323 °C to liquid phase, respectively; (3) The coexisting C- and W-type FIs are homogenized at similar temperatures of 308–340 °C and 291–343 °C, with salinities of 5.8–15.8 wt.% and 4.9–8.7 wt.% respectively.

Based on the C–H–O isotopic data and the fluid inclusion characteristics, we conclude that the ore-fluids at Xiaguan were initially derived from metamorphic devolatilization of the Qinling Group sediments (esp. carbonates), and were subsequently mixed with increasing proportion of meteoric water. Fluid boiling may have occurred in the M-stage.

7.2. Ore-forming materials source

No sulfate was discovered in the Xiaguan Ag–Pb–Zn ore field, which indicates that the fO_2 of the ore-forming fluid system was low and the sulfur in hydrothermal fluids existed mainly as HS^- and S^{2-}, and that the $\delta^{34}S$ value of pyrite (2.0 − 8.0 ‰, Table 5) would be close to that of the fluid system (Hoefs, 2004; Ohmoto and Rye, 1979). Such heavy $\delta^{34}S$ signature resembles fluid systems with a sedimentary or igneous source (Zhang, 1985; Hoefs, 2004).

On the $^{207}Pb/^{204}Pb$ vs. $^{206}Pb/^{204}Pb$ and $^{208}Pb/^{204}Pb$ vs. $^{206}Pb/^{204}Pb$ plots (Fig. 9), the ore sulfides are distributed in a domain distinct from

Table 6
Lead isotopic data of the samples from the Xiaguan Ag–Pb–Zn orefield, Erlangping Group, Qinling Group and granitic plutons in the eastern Qinling Orogen.

Location	Sample no.	Mineral	$^{206}Pb/^{204}Pb$	$^{207}Pb/^{204}Pb$	$^{208}Pb/^{204}Pb$	References
Deposit						
Yindonggou	YDG-30	Galena	18.349	15.657	38.797	This paper
	YDG-30	Pyrite	18.265	15.583	38.569	This paper
	YDG-32	Pyrite	18.347	15.654	38.771	This paper
	YDG-32	Galena	18.350	15.661	38.787	This paper
	YDG-12	Sphalerite	18.202	15.567	38.491	This paper
	YDG-12	Galena	18.343	15.669	38.812	This paper
	YDG-15	Sphalerite	18.255	15.599	38.578	This paper
	YDG-16	Sphalerite	18.388	15.730	38.943	This paper
	YDG-4	Pyrite	18.259	15.587	38.547	This paper
	YDG-4	Galena	18.333	15.666	38.780	This paper
	YDG-3	Pyrite	18.446	15.773	39.089	This paper
	YT-6	Galena	18.314	15.626	38.677	Xiang et al. (2012)
	YT-10	Galena	18.334	15.628	38.711	Xiang et al. (2012)
	YT-18	Galena	18.335	15.628	38.715	Xiang et al. (2012)
Youhulugou	YT3-2	Galena	18.254	15.618	38.566	Xiang et al. (2012)
	YT3-4	Galena	18.254	15.617	38.564	Xiang et al. (2012)
	YT10-3	Galena	18.255	15.608	38.516	Xiang et al. (2012)
	YT10-4	Galena	18.257	15.608	38.516	Xiang et al. (2012)
	YT10-6	Galena	18.278	15.616	38.534	Xiang et al. (2012)
Laozhuang	YT-45	Galena	18.236	15.618	38.543	Xiang et al. (2012)
	YT-46	Galena	18.229	15.618	38.535	Xiang et al. (2012)
	YT-51	Galena	18.236	15.617	38.541	Xiang et al. (2012)
Zhouzhuang	Z2-1	Galena	18.384	15.643	38.619	Xiang et al. (2012)
	Z2-4	Galena	18.382	15.640	38.612	Xiang et al. (2012)
	Z2-14	Galena	18.382	15.626	38.568	Xiang et al. (2012)
		Average (n = 25)	18.307	15.634	38.655	
Strata						
Erlangping Group	DM-1	Spilite	17.769	15.494	39.130	This paper
	H-2	Spilite	18.260	15.617	38.375	This paper
	H-4	Keratophyre	18.176	15.607	38.448	This paper
	X-1	Schist	18.669	15.801	39.080	This paper
	YDG-1	Schist	18.299	15.628	38.284	This paper
		Metabasalt	18.233	15.542	38.460	Zhang et al., (2002)
		Average (n = 6)	18.234	15.615	38.630	
Qinling Group	BC-14	Marble	17.494	15.405	37.378	This paper
	SCG-1	Gneiss	17.781	15.462	38.052	This paper
	S-1	Gneiss	18.608	15.636	39.418	This paper
		Gneiss	18.114	15.601	38.343	Zhang et al. (1997)
		Amphibolite	18.483	15.624	38.359	Zhang et al. (1997)
		Marble	18.312	15.571	38.168	Zhang et al., (2002)
		Average (n = 6)	18.132	15.550	38.286	
Plutons						
Erlangping		Kf in granite	17.840	15.502	37.991	Zhang et al. (1997)
		Kf in granite	17.865	15.520	38.006	Zhang et al. (1997)
		Kf in granite	17.581	15.345	37.506	Zhang et al. (1997)
Muhuding		Kf in granite	18.105	15.549	38.073	Zhang et al. (1997)
Lujiaping	YDG-8	Granite	18.972	15.581	38.592	This paper
		Average (n = 5)	18.073	15.499	38.034	

the regional plutonic units (e.g., the Erlangping granite (ca. 140 Ma), the Muhuding and Lujiaping granites (ca. 482–446 Ma)), but close to or overlap with the (meta)-sedimentary rocks of the Erlangping- and Qinling groups. Hence, the ore-forming Pb may have been sourced mainly from the sedimentary strata.

According to the studies on ore-forming elements of the other geological units in the Erlangping Terrane (Wang et al., 2003), the Xiaozhai Formation and the Yanlinggou Formation have the highest Au, Ag, Pb and Zn contents (7.46 ppb, 0.094 ppm, 35.30 ppm and 122.9 ppm respectively, Table 8) compared to other sedimentary strata or granitoids, which further support our conclusion that the metals at Xiaguan may have been sourced from the sedimentary strata.

7.3. Tectonic setting

The Qinling Orogen had experienced a multiphase tectonic evolution (Chen et al., 2009; Dong et al., 2011; Li et al., 2011; Goldfarb et al., 2014), and was likely to have multiple metallogenic events. In the Qinling Orogen, all the ca. 1.76 Ga Mo–Cu (Deng et al., 2013a, 2013b), the ca. 1.05 Ga Cu-Ni-PGE (Mi et al., 2009) and the ca. 540–410 Ma Au-Mo and Cu-Zn (Li et al., 2009; Zhang et al., 2009) metallogenic events were considered less important compared to the Mesozoic (esp. Jurassic–Cretaceous) metallogeny (Chen et al., 2009; Pirajno, 2013; Deng et al., 2014a; Deng and Wang, 2015). Precise mineralization age for the Xiaguan Ag–Pb–Zn orefield was not reported until very recently. He et al. (2015) reported the muscovite $^{40}Ar/^{39}Ar$ dating of the Y1 ore vein, and implied that the mineralization occurred not earlier than ca. 284 Ma. Our sericite $^{40}Ar/^{39}Ar$ dating constrain the metallogenetic timing to ca. 187–124 Ma (Table 7), consistent with the ore-forming age of the Banchang porphyry Cu-Au deposit in the Xiaguan Ag–Au orefield (148.1 ± 1.6 Ma, $^{40}Ar/^{39}Ar$ plateau age of K-feldspar in the ore, Li et al., 2008). Because Yindonggou is the largest deposit and there is no other age data in the study area, the metallogenic epoch of ca. 187–124 Ma is likely to represent the main ore-forming period of the Xiaguan Ag–Pb–Zn orefield, which is consistent with the large scale Mesozoic mineralization in the Qinling orogenic belt (Chen et al., 2009; Pirajno, 2013; Deng et al., 2014a; Deng and Wang, 2015).

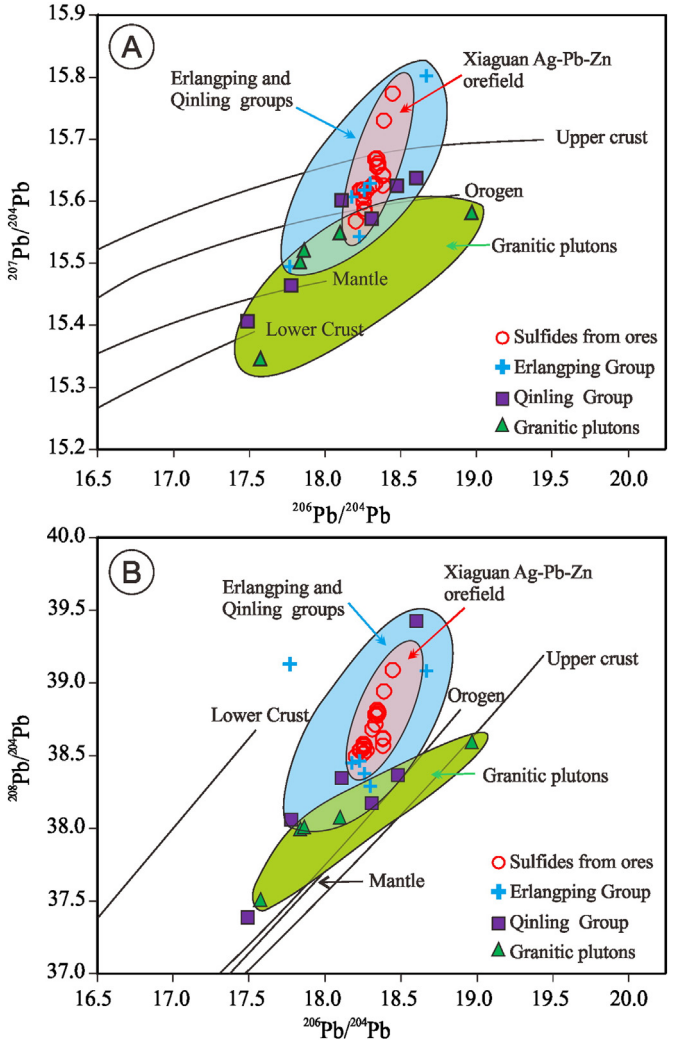

Fig. 9. Pb isotope plots of sulfides from the Xiaguan Ag–Pb–Zn orefield and related rocks. Reference lines are based on Zartman and Doe (1981) and the data are listed in Table 6.

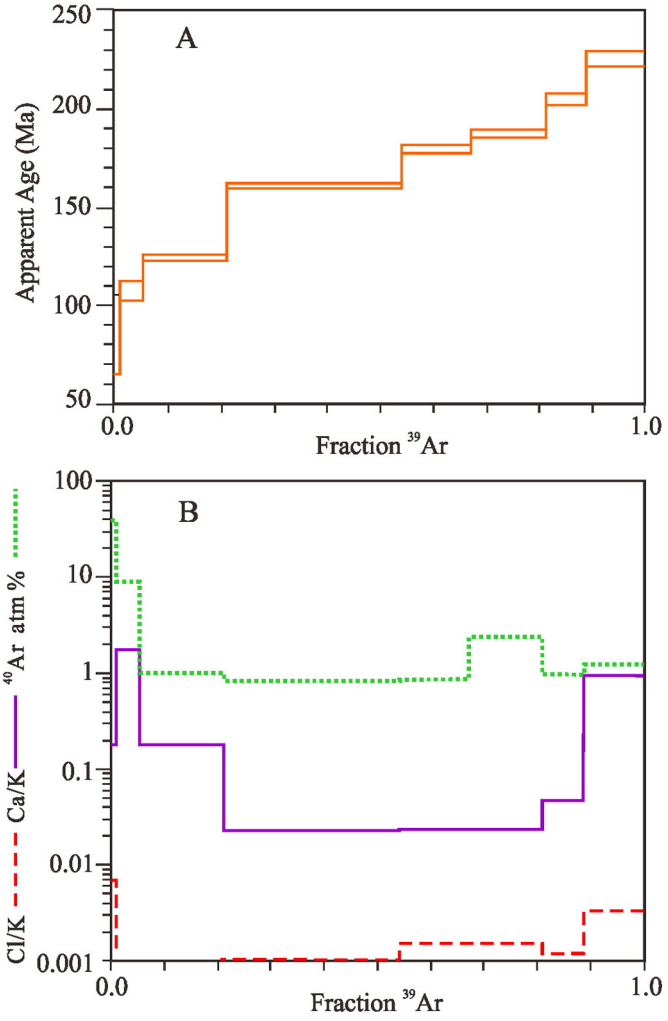

Fig. 10. (A) Conventional age-spectrum plots and (B) Cl/K, Ca/K and ^{40}Ar atm% vs. fraction ^{39}Ar diagrams for the altered sericite sample in the Yindonggou deposit.

Increasingly more evidence supports that the Yanshanian tectono-thermal event (ca. 190—90 Ma) in the Qinling–Dabie orogenic belt may have been resulted from the compressive-to-extensional transition under a continent–continent collision tectonic regime (Chen and Fu, 1992; Zhu et al., 1998; Chen et al., 2004, 2009; Pirajno, 2009; Jiang et al., 2010; Dong et al., 2012; Hu et al., 2012; Zhao et al., 2012; Zhang et al., 2013; Li et al., 2015). Thus, it is deduced that the Ag–Pb–Zn metallogenesis in the Xiaguan orefield occurred in the compression–extension transition within the intercontinental collision tectonic setting.

7.4. Ore genesis

The geological and geochemical characteristics described above show that the Yindonggou, Zhouzhuang, Laozhuang and Yinhulugou Ag–Pb–Zn deposits in the Xiaguan Ag–Pb–Zn orefield have typical features of orogenic-type deposits (Groves et al., 1998; Kerrich et al., 2000; Goldfarb et al., 2001; Chen, 2006; Chen et al., 2007 and references therein), including: (1) The Xiaguan orefield is a fault-controlled Ag–Pb–Zn belt (Chen and Fu, 1992; Wang et al., 2001), and the orebodies are controlled by subsidiary structures of the Zhu-Xia fault and occur mainly as lenticular veins, and contain dominantly quartz-sulfide vein type ores (Figs. 2, 3, 4A and B); (2) Mineralization is related to widespread and intensive silicification (Fig. 4A–C, J–L); (3) Ore-forming fluids are mesothermal, low salinity and CO_2-rich (Tables 2 and 3, Figs. 4M, N and 5). (4) From E- to L- mineralization stages, the capture pressures of FIs decrease from 280 to 320 MPa to 90–92 MPa, suggesting the metallogenic depths had become progressively shallower, and the fluid pressure had changed from lithostatic to hydrostatic value. At the same time, micro-structures of the ores and altered wallrocks had changed from compressive deformation and/or brecciation to extensional veining with open-space filling features (e.g., comb texture) (Fig. 4J–L), indicating a compressive to extensional tectonic transition in the post-collisional Qinling Mountains.

To conclude, our evidence supports that the Xiaguan Ag–Pb–Zn orefield is best classified as an orogenic-type metallogenic system.

7.5. Metallogenic process

Integrating evidence from regional tectonics, lithology, metamorphism and ore-forming fluids, we propose a tectono-metallogenic model for the Xiaguan Ag–Pb–Zn orefield (Fig. 11): During the Mesozoic continent–continent collision of the Yangtze and North China blocks, the southern Qinling terrane may have subducted northward beneath the northern Qinling terrane along the Shang-Dan fault belt (Fig. 1). According to the CMF model (Chen et al., 2004; Pirajno, 2009), the subducted sediments, including the Qinling carbonates and the Erlangping flysch, may have been metamorphosed, devolatilized or even partially melted, thus providing the CO_2-rich ore-fluids with relatively elevated carbon and oxygen isotope compositions for the Xiaguan ore-forming system (Fig. 11). During the migration, circulation and

Table 7
$^{40}Ar/^{39}Ar$ analysis of the sericite from altered tectonite in the Y1 orebody, Yindonggou deposit.

Power	$^{36}Ar/^{40}Ar \pm 2\sigma$	$^{39}Ar/^{40}Ar \pm 2\sigma$	^{40}Ar atm%	^{39}Ar%	$^{40}Ar^*/^{39}K \pm 2\sigma$	Age $\pm 2\sigma$(Ma)
0.75	0.001309 ± 0.000487	0.091687 ± 0.003422	38.56	1.17	6.690 ± 1.605	85.62 ± 20.06
1.50	0.000303 ± 0.000143	0.107461 ± 0.001252	8.93	4.28	8.472 ± 0.405	107.76 ± 5.01
3.00>	0.000034 ± 0.000038	0.100605 ± 0.000623	1.00	15.67	9.840 ± 0.128	124.56 ± 1.56
4.50>	0.000029 ± 0.000015	0.077188 ± 0.000405	0.84	33.05	12.846 ± 0.089	160.97 ± 1.06
5.00>	0.000029 ± 0.000031	0.068762 ± 0.000520	0.86	13.00	14.417 ± 0.171	179.71 ± 2.03
6.00>	0.000080 ± 0.000031	0.064643 ± 0.000443	2.37	13.75	15.102 ± 0.176	187.81 ± 2.08
7.00>	0.000033 ± 0.000042	0.059723 ± 0.000514	0.97	7.92	16.581 ± 0.251	205.20 ± 2.94
7.00>	0.000042 ± 0.000029	0.053840 ± 0.000768	1.23	11.16	18.345 ± 0.308	225.72 ± 3.56

Table 8
Metal element contents of the strata and intrusions in the Erlangping Terrane (Wang et al., 2003).

Strata	Sample number	Au (10^{-9})	Ag (10^{-6})	Pb (10^{-6})	Zn (10^{-6})	Cu (10^{-6})	As (10^{-6})	Sb (10^{-6})	Bi (10^{-6})
Erlangping Group									
Xiaozhai Formation	12	5.90	0.094	35.30	122.9	41.90	3.7	1.0	0.61
Huoshenmiao Formation	28	3.61	0.058	17.60	61.60	36.60	2.3	0.5	0.50
Damiao Formation	9	1.77	0.055	17.60	85.30	45.00	5.5	0.7	0.50
Qinling Group									
Yanlinggou Formation	15	7.46	0.080	–	–	–	3.6	0.7	1.38
Plutons									
570–410 Ma granite	57	1.35	0.050	–	–	–	2.2	0.5	0.36

interaction with the country rocks, hydrothermal fluids in Xiaguan may have extracted ore-forming elements from the obducted side (mainly the Erlangping Group), and then transported them into structural traps favorable for ore deposition (e.g., subsidiary faults of Zhu-Xia fault or the bedding faults in the Erlangping Group). Consequently, ore sulfides may have inherited the isotopic characteristics of the Erlangping Group, especially the low $^{207}Pb/^{204}Pb$ and high $^{208}Pb/^{204}Pb$. Therefore, E-stage ore fluids may have been originated from metamorphic dehydration. With the tectonics changed from compressive to extensional, ductile-deformed structures expanded and became brittle and open, and thereby facilitating fluid circulation and ore metal precipitation. The opening of these structures may have also facilitated phase separation or fluid boiling, together with the mixing with circulating meteoric water, resulting in further precipitation of ore metals. In this way, the Xiaguan ore fluid system changed from metamorphic to meteoric.

The occurrence of thick carbonate veins in Yindonggou, Zhuzhuang and other Ag–Pb–Zn deposits coincides with the L-stage extensional structures. The concealed Songduo granite pluton ca. 3–4 km north of the ore district (HINME, Henan Institute of Nonferrous Metal Exploration, 2003) are probably the products of metamorphism and liquation during the further subduction processes of the underthrusted materials.

8. Conclusion

Regional geology, ore geology and fluid system of the fault-controlled Xiaguan Ag–Pb–Zn orefield coincide with the characteristics of typical orogenic-type deposits summarized in previous studies. The $^{40}Ar/^{39}Ar$ isotope ages constrain the formation time of these Ag–Pb–Zn deposits to the Early Jurassic–Early Cretaceous (ca. 187 — 124 Ma). This shows that the Xiaguan metallogenesis coincided with a regional compression to extension transition led by the uplifting of the Qinling orogen. The Yindonggou, Zhouzhuang and other Ag deposits in study area are typical of orogenic-type Ag deposits formed in a continent–continent collision tectonic regime.

Silver deposits at Xiaguan were formed by a mesothermal, CO_2-rich, low density and dilute, Na^+–Cl^--type fluid-system. From the E- to L- ore-forming stages, metallogenic depths had become progressively shallower, and the fluid-pressure changed from lithostatic to hydrostatic

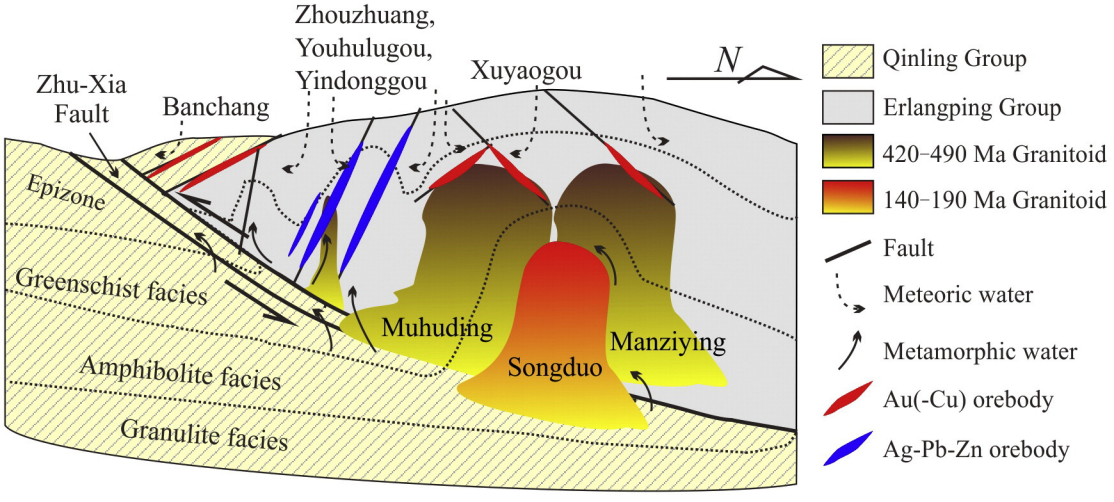

Fig. 11. Tectono-metallogenic model for the Xiaguan Ag–Pb–Zn orefield.

value. Our studies on H–O–C isotopic systematics imply that the E-stage fluids were sourced from metamorphic devolatilization of marine carbonates, whereas L-stage fluids contain a significant component of meteoric water. The marble-containing Qinling Group south of the ore district may have contributed to the E-stage ore-forming fluids.

Consequently, we suggest that the Qinling Group may have underthrusted northward beneath the Erlangping Terrane along the Zhu-Xia fault during the Mesozoic collision between the Yangtze and North China blocks. The down-going slab may have progressively devolatilized through metamorphism, resulting in the development of orogenic-type ore fluid system. Subsequently, the ore fluids may have precipitated at the ductile-to-brittle transition stage in structural traps, forming the Yindonggou, Zhouzhuang and other Ag-dominated polymetallic deposits.

Acknowledgments

This research was co-funded by the National Nature Science Foundation of China (No. 41030423), the Fundamental Research Funds for the Central Universities (No. 2652013017) and the 111 Project (B07011). Our especial thanks go to Senior Engineer Wang Jianming for assisting the field work and to Professor Chen Huayong for helping with the $^{40}Ar/^{39}Ar$ isotope dating. Two anonymous reviewers are thanked for their critical reviews and constructive comments. Cenozoic Geoscience Editing is acknowledged for their language polishing and scientific editing services.

References

Bodnar, R.J., 1993. Revised equation and stable for determining the freezing point depression of $H_2O-NaCl$ solutions. Geochim. Cosmochim. Acta 57, 683–684.
Brown, P.E., Lamb, W.M., 1989. P-V-T properties of fluids in the system H_2O-CO_2-NaCl: new graphical presentations and implications for fluid inclusion studies. Geochim. Cosmochim. Acta 53, 1209–1221.
Brown, P.E., 1989. Flincor: a microcomputer program for the reduction and investigation of fluid-inclusion data. Am. Mineral. 74, 1390–1393.
Cao, J.H., Xiang, S.H., Xue, C.J., Zhang, X., Li, Y.F., Li, B.Q., Cheng, W.H., 2011. Ore geology and ore-forming fluid geochemistry of Zhouzhuang Ag–Pb–Zn deposit, southwestern Henan Province. Front Earth Sci. 18, 159–171 (in Chinese with English abstract).
Chacko, T., Mayeda, T.K., Clayton, R.N., Goldsmith, J.R., 1991. Oxygen and carbon isotope fractionations between CO_2 and calcite. Geochim. Cosmochim. Acta 55, 2867–2882.
Chen, H.Y., Chen, Y.J., Baker, M.J., 2012. Evolution of ore-forming fluids in the Sawayaerdun gold deposit in the Southwestern Chinese Tianshan metallogenic belt, Northwest China. J. Asia Earth Sci. 49, 131–144.
Chen, H.Y., Chen, Y.J., Liu, Y.L., 2001. Metallogenesis of the Ertix gold belt, Xinjiang and its relationship to Central Asia-type orogenesis. Sci. China Ser. D 44, 245–255.
Chen, Y.J., 2006. Orogenic-type deposits and their metallogenic model and exploration potential. Geol. China 33, 1181–1196 (in Chinese with English abstract).
Chen, Y.J., Fu, S.G., 1992. Gold Mineralization in West Henan, China. Seismological Press, Beijing (234 pp., in Chinese with English abstract).
Chen, Y.J., Ni, P., Fan, H.R., Pirajno, F., Lai, Y., Su, W.C., Zhang, H., 2007. Diagnostic fluid inclusions of different types of hydrothermal gold deposits. Acta Petrol. Sin. 23, 2085–2108 (in Chinese with English abstract).
Chen, Y.J., Pirajno, F., Qi, J.P., 2005. Origin of gold metallogeny and sources of ore-forming fluids, in the Jiaodong province, eastern China. Int. Geol. Rev. 47, 530–549.
Chen, Y.J., Pirajno, F., Sui, Y.H., 2004. Isotope geochemistry of the Tieluping silver deposit, Henan, China: a case study of orogenic silver deposits and related tectonic setting. Mineral Deposits 39, 560–575.
Chen, Y.J., Zhai, M.G., Jiang, S.Y., 2009. Significant achievements and open issues in study of orogenesis and metallogenesis surrounding the North China continent. Acta Petrol. Sin. 25, 2695–2726 (in Chinese with English abstract).
Chen, Y.L., Yang, Z.F., Zhang, H.F., Ling, W.L., 1996. Geochemical characteristics of Sr, Nd and Pb isotopes of late Paleozoic-Mesozoic granitoids from Northern Qinling belt. Earth Sci. J. China Univ. Geosci. 21, 27–32 (in Chinese with English abstract).
Clark, A.H., Archibald, D.A., Lee, A.W., 1998. Laser probe $^{40}Ar/^{39}Ar$ ages of early- and late-stage alteration assemblages, Rosario porphyry copper-molybdenum deposit, Collahuasi District, I Region, Chile. Econ. Geol. 93, 326–337.
Clayton, R.N., O'Neil, J.L., Mayeda, T.K., 1972. Oxygen isotope exchange between quartz and water. J. Geophys. Res. 77, 3057–3067.
Collins, P.L.F., 1979. Gas hydrates in CO_2-bearing fluid inclusions and the use of freezing data for estimation of salinity. Econ. Geol. 74, 1435–1444.
Deng, J., Wang, Q.F., 2015. Gold mineralization in China: metallogenic provinces, deposit types and tectonic framework. Gondwana Res. http://dx.doi.org/10.1016/j.gr.2015.10.003.
Deng, J., Gong, Q., Wang, C., Carranza, E.J.M., Santosh, M., 2014a. Sequence of Late Jurassic–Early Cretaceous magmatic–hydrothermal events in the Xiong'ershan region, Central China: an overview with new zircon U–Pb geochronology data on quartz porphyries. J. Asia Earth Sci. 79, 161–172.
Deng, J., Liu, X.F., Wang, Q.F., Pan, R.G., 2015. Origin of the Jiaodong-type Xinli gold deposit, Jiaodong Peninsula, China: constraints from fluid inclusion and C–D–O–S–Sr isotope compositions. Ore Geol. Rev. 65, 674–686.
Deng, X.H., Chen, Y.J., Santosh, M., Yao, J.M., 2013a. Genesis of the 1.76 Ga Zhaiwa Mo–Cu and its link with the Xiong'er volcanics in the North China Craton: implications for accretionary growth along the margin of the Columbia supercontinent. Precambrian Res. 227, 337–348.
Deng, X.H., Chen, Y.J., Santosh, M., Zhao, G.C., Yao, J.M., 2013b. Metallogeny during continental outgrowth in the Columbia supercontinent: isotopic characterization of the Zhaiwa Mo–Cu system in the North China Craton. Ore Geol. Rev. 51, 43–56.
Deng, X.H., Santosh, M., Yao, J.M., Chen, Y.J., 2014b. Geology, fluid inclusions and sulfur isotopes of the Zhifang Mo deposit in Qinling Orogen, central China: a case study of orogenic-type Mo deposits. Geol. J. 49, 515–533.
Dong, Y., Genser, J., Naebauer, F., Zhang, G., Liu, X., Yang, Z., Heberer, B., 2011. U–Pb and $^{40}Ar/^{39}Ar$ geochronological constraints on the exhumation history of the North Qingling terrane, China. Gondwana Res. 19, 881–893.
Dong, Y.P., Liu, X.M., Neubauer, F., Zhang, G.W., Tao, N., Zhang, Y.G., Zhang, X.N., Li, W., 2013. Timing of Paleozoic amalgamation between the North China and South China Blocks: evidence from detrital zircon U–Pb ages. Tectonophysics 586, 173–191.
Dong, Y.P., Liu, X.M., Zhang, G.W., Chen, Q., Zhang, X.N., Li, W., Yang, C., 2012. Triassic diorites and granitoids in the Foping area: constraints on the conversion from subduction to collision in the Qinling orogen, China. J. Asian Earth Sci. 47, 123–142.
Faure, G., 1986. Principles of Isotope Geology. second ed. John Wiley and Sons, New York (589 pp.).
Fu, X., Men, D.G., Qin, Z., Wang, H.L., Zuo, J., Fu, H.J., Han, J., Wen, S.H., 2011. Geology feature and genesis of Lujiaping silver–gold polymetallic ore deposit, Henan. Miner. Explor. 2, 536–543 (in Chinese with English abstract).
Goldfarb, R.J., Groves, D.I., Cardoll, S., 2001. Orogenic gold and geologic time: a global synthesis. Ore Geol. Rev. 18, 1–75.
Goldfarb, R.J., Taylor, R.D., Collions, G.S., Goryachev, N.A., Orlandini, O.F., 2014. Phanerozoic continental growth and gold metallogeny of Asia. Gondwana Res. 25, 48–102.
Groves, D.I., Goldfarb, R.J., Gebre-Mariam, M., Hagemann, S.G., Robert, F., 1998. Orogenic gold deposits: a proposed classification in the context of their crustal distribution and relationship to other gold deposit types. Ore Geol. Rev. 13, 7–27.
Guo, C.L., Chen, D.L., Fan, W., Wang, A.G., 2010. Geochemical and zircon U–Pb chronological studies of the Manziying granite in Erlangping area, western Henan Province. Acta Petrol. Mineral. 29, 15–22 (in Chinese with English abstract).
Hagemann, S.G., Luders, V., 2003. P–T–X conditions of hydrothermal fluids and precipitation mechanism of stibnite-gold mineralization at the Wiluna lode-gold deposits, Western Australia: conventional and infrared microthermometric constraints. Mineral Deposits 38, 936–952.
HBGR (Henan Bureau of Geology and Resource), 1989. The Regional Geology of Henan Province. Geological Publishing House, Beijing (772 pp., in Chinese).
He, W.P., Ren, D.D., Cao, J.H., 2015. $^{40}Ar/^{39}Ar$ dating of muscovite from altered rocks of Yindonggou Ag–Pb–Zn deposit in southwest of Henan. Miner. Resour. Geol. 29 (3), 402–407 (in Chinese with English abstract).
HINME (Henan Institute of Nonferrous Metal Exploration), 2003. The Evaluation for Ag–Cu–Pb Deposits in Neixiang–Nanzhao Area, Henan Province. Unpublished, Zhengzhou (33 pp., in Chinese).
Hoefs, J., 2004. Stable Isotope Geochemistry. fifth ed. Springer-Verlag, Berlin (201 pp.).
Hu, J., Jiang, S.Y., Zhao, H.X., Shao, Y., Zhang, Z.Z., Xiao, E., Wang, Y.F., Dai, B.Z., Li, H.Y., 2012. Geochemistry and petrogenesis of the Huashan granites and their implications for the Mesozoic tectonic settings in the Xiaoqinling gold mineralization belt, NW China. J. Asia Earth Sci. 56, 276–289.
Hu, S.X., Lin, Q.L., Chen, Z.M., 1988. Geology and Metallogeny of the Collision Belt Between the North and the South China Plates. Nanjing University Press, Nanjing (558 pp., in Chinese).
Jiang, S.Y., Dai, B.Z., Jiang, Y.H., Zhao, H.X., Hou, M.N., 2009. Jiaodong and Xiaoqinling: two orogenic gold provinces formed in different tectonic settings. Acta Petrol. Sin. 25, 2727–2738 (in Chinese with English abstract).
Jiang, Y.H., Jin, G.D., Liao, S.Y., Zhou, Q., Zhao, P., 2010. Geochemical and Sr–Nd–Hf isotopic constraints on the origin of Late Triassic granitoids from the Qinling orogen, central China: implications for a continental arc to continent–continent collision. Lithos 117, 183–197.
Kerrich, R., Goldfarb, R.J., Groves, D.I., Garwin, S., Jia, Y., 2000. The characteristics, origins and geodynamic settings of supergiant gold metallogenic provinces. Sci. China Ser. D 43, 1–68.
Li, H.M., Wang, D.H., Guo, B.J., Chen, Y.C., Bai, F.J., Qiu, J.J., 2008. $^{40}Ar-^{39}Ar$ age of potash feldspar from the Banchang Ag–Cu–Pb–Zn–(Mo) deposit in Henan and its geological significance. Acta Geosci. Sin. 29, 154–160 (in Chinese with English abstract).
Li, J., Qiu, J.J., Sun, Y.L., 2009. Re–Os isotope dating of the Yindonggou Ag–Au–Mo deposit, Henan province and its implication for Caledonian orogenic–metallogenic event. Acta Petrol. Sin. 25, 2763–2768 (in Chinese with English abstract).
Li, N., Chen, Y.J., Fletcher, I.R., Zeng, Q.T., 2011. Triassic mineralization with cretaceous overprint in the Dahu Au–Mo deposit, Xiaoqinling gold province: constraints from SHRIMP monazite U–Th–Pb geochronology. Gondwana Res. 20, 543–552.
Li, N., Chen, Y.J., Santosh, M., Pirajno, F., 2015. Compositional polarity of Triassic granitoids in the Qinling orogen, China: implication for termination of the northernmost paleo-Tethys. Gondwana Res. 27, 244–257.
Li, N., Chen, Y.J., Zhang, H., Zhao, T.P., Deng, X.H., Wang, Y., Ni, Z.Y., 2007. Molybdenum deposits in East Qinling. Earth Sci. Front. 14, 186–198 (in Chinese with English abstract).
Li, S.L., Yao, J.J., Wu, Q.J., Li, Y.Q., Zhang, D.H., 2012. Typical ore deposit spots in Tuanyuan silver poly-metallic ore assembly area in southwest of Henan province: evidence

from ore geology, fluid characteristics and zircon U–Pb dating. Geol. Bull. China 31, 1608–1627 (in Chinese with English abstract).
Mi, M., Chen, Y.J., Sun, Y.L., Wang, Y., Jiang, H.Z., 2009. Rare earth element and platinum-group element and platinum-group element geochemistry of the Zhou'an Ni–Cu–PGE deposit in Henan province: implications for hydrothermal origin. Acta Petrol. Sin. 25, 2769–2775 (in Chinese with English abstract).
Nance, R.D., Murphy, J.B., Santosh, M., 2014. The supercontinent cycle: a retrospective essay. Gondwana Res. 25, 4–29.
Ni, Z.Y., Chen, Y.J., Li, N., Zhang, H., 2012. Pb–Sr–Nd isotope constraints on the fluid source of the Dahu Au–Mo deposit in Qinling Orogen, central China, and implication for Triassic tectonic setting. Ore Geol. Rev. 46, 60–67.
Ohmoto, H., Rye, R.O., 1979. Isotopes of sulfur and carbon. In: Barnes, H.L. (Ed.), Geochemistry of Hydrothermal Ore Deposits, second ed. Wiley, New York, pp. 509–567.
Pirajno, F., 2009. Hydrothermal Processes and Mineral Systems. Springer, Berlin (1250 pp.).
Pirajno, F., 2013. The Geology and Tectonics Settings of China's Mineral Deposits. Springer, Berlin (679 pp.).
Schidlowski, M., 1998. Beginning of terrestrial life: problems of the early record and implications for extraterrestrial scenarios. Instruments, Methods, and Missions for Astrobiology, SPIE 3441, pp. 149–157.
Sibson, R.H., Robert, F., Poulsen, H., 1988. High angle reverse faults, fluid pressure cycling and mesothermal gold quartz deposits. Geology 16, 551–555.
Taylor, H.P., 1974. The application of oxygen and hydrogen isotope studies to problems of hydrothermal alteration and ore deposition. Econ. Geol. 69, 843–883.
Tu, G.Z., Ding, K., 1986. The Qinling-Central Asia Sb–Hg belt—the third Sb–Hg belt of global significance. Geochemical CollectionsInstitute of Geochemistry, China Academy of Sciences. Science Press, Beijing, pp. 8–13 (in Chinese with English abstract).
Wang, H., Wu, Y., Gao, S., Zheng, J., Liu, Q., Liu, X., Qin, Z., Yang, S., Gong, H., 2014. Deep subduction of continental crust in accretionary orogen: evidence from U–Pb dating on diamond-bearing zircons from the Qinling orogen, central China. Lithos 190–191, 420–429.
Wang, Z.G., Liu, X.D., Zhang, Z.B., 2001. The metallogenic condition and prospecting foreground of the silver poly-metals deposits in Erlangping Terrane in East Qinling Orogen. Chin. Geol. 28, 32–36 (in Chinese).
Wang, Z.G., Xiang, S.H., Liu, X.D., Zhang, Z.B., 2003. Geological character of Yindonggou large scale silver and gold poly metallic deposit in Henan province and it's discovery process and geological signification. Miner. Res. Geol. 17, 365–368 (in Chinese with English abstract).
Wei, H.M., Jiao, J.G., Yang, F.C., 2003. The features of Muhuding granite and its relation to gold deposits in Neixiang Henan. J. Chang'an Univ. Earth Sci. 25, 1–6 (in Chinese with English abstract).
Xiang, S.H., Cao, J.H., Xue, C.J., Zhang, X., Li, Y.F., Li, B.Q., Wang, X.Y., 2012. S and Pb isotopic constraints on the ore-forming material sources of the Pb–Zn–Ag ore deposit in Northern Neixiang, Henan Province. Geoscience 26, 464–470 (in Chinese with English abstract).
Zartman, R.E., Doe, B.R., 1981. Plumbotectonics — the model. Tectonophysics 75, 135–162.
Zhai, M.G., Santosh, M., 2013. Metallogeny of the North China Craton: link with secular changes in the evolving Earth. Gondwana Res. 24, 275–297.
Zhang, B.R., Gao, S., Zhang, H.F., 2002. Geochemistry of Qinling Orogen. Science Press, Beijing (187 pp., in Chinese with English abstract).
Zhang, H.F., Gao, S., Zhang, B.R., Luo, T.C., Lin, W.L., 1997. Pb isotopes of granitoids suggests Devonian accretion of Yangtze (South China) craton to North China craton. Geology 25, 1015–1018.
Zhang, J., Chen, Y.J., Li, G.P., Li, Z.L., Wang, Z.G., 2004. Characteristics of ore geology and fluid inclusion of the Yindonggou silver deposit, Neixiang county, Henan province: implication for metallogenic type. J. Mineral. Petrol. 24, 55–64 (in Chinese with English abstract).
Zhang, J., Chen, Y.J., Pirajno, F., Deng, J., Chen, H.Y., Wang, C.M., 2013. Geology, C–H–O–S–Pb isotope systematics and geochronology of the Yindongpo gold deposit, Tongbai Mountains, central China: implication for ore genesis. Ore Geol. Rev. 53, 343–356.
Zhang, J., Chen, Y.J., Qi, J.P., Ge, J., 2009. Comparison on the typical metallogenic systems in the north slope of Tongbai–East Qinling Mountains and its geologic implications. Acta Geol. Sin. 83, 396–410.
Zhang, J., Li, L., Gilbert, S., Liu, J., Shi, W., 2014. LA–ICP-MS and EPMA studies on the Fe–S–As minerals from the Jinlongshan gold deposit, Qinling Orogen, China: implications for ore-forming processes. Geol. J. 49, 482–500.
Zhang, L., Chen, H.Y., Chen, Y.J., Qin, Y.J., Liu, C.F., Zheng, Y., Jansen, N.H., 2012. Geology and fluid evolution of the Wangfeng orogenic-type gold deposit. Ore Geol. Rev. 49, 85–95.
Zhang, L.G., 1985. The Application of Stable Isotope in Geological Science. Shaanxi Science and Technology Press, Xi'an (267 pp., in Chinese).
Zhang, L.G., 1989. Petrogenic and Minerogenic Theories and Prospecting. Beijing University of Technology Press, Beijing (200 pp., in Chinese with English abstract).
Zhao, G.C., Sun, M., Wilde, S.A., Li, S.Z., 2004. A paleo-Mesoproterozoic supercontinent: assembly, growth and breakup. Earth Sci. Rev. 67, 91–123.
Zhao, H.X., Hartwig, E.F., Jiang, S.Y., Dai, B.Z., 2011. LA-ICP-MS trace element analysis of pyrite from the Xiaoqinling gold district, China: implications for ore genesis. Ore Geol. Rev. 43, 142–153.
Zhao, H.X., Jiang, S.Y., Hartwig, E.F., Da, I.B.Z., Ma, L., 2012. Geochemistry, geochronology and Sr–Nd–Hf isotopes of two Mesozoic granitoids in the Xiaoqinling gold district: implication for large-scale lithospheric thinning in the North China Craton. Chem. Geol. 294–295, 173–189.
Zheng, Y., Zhang, L., Chen, Y.J., Qin, Y.J., Liu, C.F., 2012. Geology, fluid inclusion geochemistry and $^{40}Ar/^{39}Ar$ geochronology of the Wulasigou Cu deposit in Altay, Xinjiang, China and their implications for ore genesis. Ore Geol. Rev. 49, 128–140.
Zhou, Z.J., Chen, Y.J., Jiang, S.Y., Zhao, H.X., Qin, Y., Hu, C.J., 2014. Geology, geochemistry and ore genesis of the Wenyu gold deposit, Xiaoqinling gold field, Qinling Orogen, southern margin of North China Craton. Ore Geol. Rev. 59, 1–20.
Zhu, R.X., Yang, Z.Y., Wu, H.N., Ma, X.H., Huang, B.C., Meng, Z.F., Fang, D.J., 1998. Paleomagnetic constrains on the tectonic history of the major blocks of China during the Phanerozoic. Sci. China Ser. D 41, 1–19 (sup.).